Theory of nonlocal modal hydrodynamic functions for beam and plate vibrations in viscous fluids

Burak Gulsacan^a, Matteo Aureli^{a,*}

^aMechanical Engineering Department, University of Nevada, Reno 1664 N. Virginia Street, Reno, NV 89557-0312, USA

Abstract

In this paper, we introduce a new nonlocal modal hydrodynamic theory for fluid-structure interactions (FSI) of light, flexible cantilever beams and plates undergoing small amplitude vibrations in Newtonian, incompressible, viscous, heavy fluids otherwise at rest. For low aspect ratio flexible structures and high mode numbers, three dimensional (3D) and nonlocal fluid effects become prominent drivers of the coupled dynamics, to the point that existing local hydrodynamic theories based on two dimensional (2D) fluid approximations become inadequate to predict the system response. On the other hand, our approach is based on a rigorous, yet efficient, 3D treatment of the hydrodynamic loading on cantilevered thin structures. The off-line solution of the FSI problem results in the so-called nonlocal modal hydrodynamic function matrix, that is, the representation of the nonlocal hydrodynamic load operator on a basis formed by the structural modes. Our theory then integrates the nonlocal hydrodynamics within a fully coupled structural modal model in the frequency domain. We compare and discuss our theory predictions in terms of frequency response functions, mode shapes, hydrodynamic loads, quality factors, added mass ratios with the predictions of the classical local approaches, for different actuation scenarios, identifying the limitations of the hypotheses underlying existing treatments. Importantly, we also validate our new model with experiments conducted on flexible square plates. While computationally efficient, our fully coupled theory is exact up to numerical truncation and can bridge knowledge gaps in the design and analysis of FSI systems based on low aspect ratio flexible beams and plates.

Keywords: Hydrodynamic function, Unsteady Stokes flow, Boundary element methods, Underwater beam and plate vibrations

Nomenclature

- α Frequency parameter in unsteady Stokes flow
- β Nondimensional frequency parameter
- ζ Vorticity vector
- **D** Integration domain
- e_i Unit reference frame vector
- f Modal forcing
- H Nonlocal modal hydrodynamic function matrix and entries
- I Identity matrix
- K, M Stiffness and mass matrix of the structure
- n Normal unit vector
- N_0, N_1, N_2 Coefficients matrices in asymptotic expansions

- q Modal coefficients
- *r* Distance vector*u* Velocity vector
- u velocity vector
- x, \bar{x} Position vector
- δ_{ij} Kronecker delta
- η Structural damping coefficient
- Γ Local hydrodynamic function
- γ_{ij} Coherence factor
- Phasor of variable
- Λ Aspect ratio of the cantilever
- λ_i Eigenvalue of the in-vacuo modes
- $\mathcal{A}, A(R), B(R), C(R), D(R)$ Singularity tensors
- $\mathcal{A}_0, \mathcal{A}_1, \mathcal{A}_2$ Singularity tensors (asymptotic analysis)

^{*}Corresponding author. Tel.: +1-775-784-6973. Fax: +1-775-784-1701. Email address: maureli@unr.edu (Matteo Aureli)

 \mathcal{F}_{ext} General external forcing

 \mathcal{H}_{ω} Nonlocal hydrodynamic operator

K, M Linear operators describing stiffness and inertia

R Mass ratio

 W_H Work done by the hydrodynamic forces on the cantilever

KC Keulegan-Carpenter number

ν Poisson's ratio of the structure

ω Radian frequency

 ω_d, ω_w Dry and wet resonance frequency

 ω_p Frequency of the peak response

 $\Phi^I, \phi_i, \varphi_i$ Basis modes

 Ψ^d, Ψ^w Dry and wet mode shapes

 ρ_f, μ_f Fluid density and dynamic viscosity

 ρ_s Solid density

 $\sigma_{ij}, \epsilon_{ij}$ Stress and strain components

 τ_{jk} , [[τ]] Fluid stress tensor and traction jump

Nondimensional or scaled variable

 ε_{kji} Levi-Civita symbol

A Cross-section area

A₀ Amplitude of oscillation

b, L, h Width, length, and thickness of cantilever

 C_i Scaling constant for dry(in-vacuo) modes of the fixed-free cantilever

 c_{ij}, C_{ijkl} Coefficients of the elastic tensor

 D, D_{ij} Plate flexural rigidity

E, E' Young's modulus (plane stress/strain) of the cantilever

 E_i, G_{ij}, v_{ij} Elastic coefficients

 f^+, f_0 Nondimensional frequency and scaling

 f_n Natural frequency

G Shear Modulus

 h_{ij} ij-entry of the nonlocal modal hydrodynamic function matrix

 I, J_t Moment of inertia and polar moment of inertia

 M_A , Q Added mass coefficient and quality factor

p Pressure

R Argument of singularity tensors

 S_{ij}, Ω_{ij} Oscillatory Stokeslet and rotlet tensors

t Time

T, U Kinetic and potential energy

 w, θ Transverse displacement and rotation field

 W_B, Θ_B Measured rigid translation and rigid rotation angle

 W_C Measured elastic motion of the corner of the cantilever

1. Introduction

Over the past few decades, the fluid-structure interaction (FSI) community has witnessed increasing research interest in the study of dynamics and vibrations of submerged slender cantilever beam systems. These problems are relevant in a number of important engineering applications such as atomic force microscopy [1, 2, 3, 4], sensing and actuation in microelectromechanical systems (MEMS) [5, 6, 7, 8], bio-inspired and/or robotic underwater propulsion [9, 10, 11, 12, 13], piezoelectric-based cooling and flow control [14, 15, 16, 17], and energy harvesting systems [18, 19, 20, 21]. In many of these works, rather than resorting to a fully coupled three dimensional (3D) FSI simulation, researchers have adopted the influential solution strategy of Tuck [22] and Sader [1] which is based on the so-called complex hydrodynamic function formalism. Here, the assumption is that, at any location along the beam axis, the hydrodynamic load is only dependent on the local transverse displacement of the beam and the vibration frequency. Under this hypothesis, a local two dimensional (2D) unsteady Stokes flow is postulated in the plane orthogonal to the beam axis and is used to calculate the local hydrodynamic load, typically via a boundary element method approach [22]. The resulting load is described in terms of a complex hydrodynamic function that is then included in structural dynamics models to predict the response of the system, see [1].

This, now classical, approach has enjoyed immense success and popularity for the prediction of the first few flexural resonance frequencies and quality factors of slender submerged cantilever beams in the linear hydrodynamics regime. Notably, this line of work also extended, to viscous fluids, the influential results of Chu [23] that can be used to quickly and accurately estimate the added mass effect, or frequency shift of the wet resonance modes, for high-frequency vibrations of beams in inviscid fluids. This local hydrodynamic approach has enabled many technical and scientific advancements in various linear FSI problems, including the investigation of torsional vibrations [24], the effect of near-wall [25] or free-surface [26] presence, and the effect of different cross section geometries of oscillating cantilever structures [27]. The basic formalism was also extended, via suitable correction terms, to the treatment of moderately large bending vibrations, where the effect of fluid nonlinearities and vortex shedding are taken into

account [16, 28, 29, 30].

Although the local theory has been proved to be very successful in the context of the hydrodynamic characteristics of vibrating slender beams, it is also known [1] that some of its hypotheses are inadequate when the analysis is concerned with low aspect ratio flexible structures (i.e. short cantilevers), vibrating at high mode numbers [31, 32, 33, 34, 35, 36, 37]. Lindholm *et al.* [31] were among the first researchers to propose experimental corrections on lower aspect ratios by enhancing Chu's fundamental study [23]. More recently, Atkinson and de Lara [32] conducted a FSI study on the vibrations of a wide rectangular cantilever plate in a viscous fluid, revealing a nonlocal dependence of hydrodynamic loading on the mode shape. Shen *et al.* [34] expanded on [32] by considering different clamping conditions, demonstrating drastic changes on the dynamic response of the vibrating cantilevered structures resulting from the nonlocal behavior of the flow. Other groups focused on corrections to the local hydrodynamic function formalism to take into account finite aspect ratios and end effects. For example, Facci and Porfiri [33] performed a parametric numerical study using the finite volume method on the underwater vibrations of a cantilever beam extending the accuracy of the nonlinear formalism of [29] to lower aspect ratios. Of note, hydrodynamic damping and mean thrust trends were shown in [33] to substantially differ for low aspect ratio cases, from the local fluid approximations.

Due to increasing interest in plate geometries for high sensitivity, tunable sensing applications [38, 39, 40, 41, 42], several research groups are actively working to bridge the knowledge gaps in the theory and practice of vibrations of low aspect ratio cantilevered structures in viscous fluids. Among those, we highlight the contributions of Gesing et al. [36, 35] that, while employing a local hydrodynamic theory, studied the excitation and dynamic response of non-conventional plate-like modes, extracting the displacement spectra through a strip-like integration of the 2D hydrodynamics along the axis of the structure. While these works introduce complex plate-like mode shapes in the analysis, the solution of the hydrodynamic problem is still based on a 2D fluid treatment and therefore is expected to be somewhat incomplete for very low aspect ratio plate-like systems vibrating at high mode number. Note also that the local hydrodynamic method, adapted from [1, 22], is based on prescribed mode shapes for the solid structures for the calculation of the hydrodynamic field which may not be accurate representations of the way the solid is actually vibrating. Similarly, complex plate-like mode shapes were also previously considered, with a local 2D, although nonlinear, hydrodynamic treatment in our group's work on underwater vibrations of shape-morphing structures [43, 44, 45]. Nonlocality and the effect of low aspect ratio were addressed in part in [46], via linear 3D flow simulations based on boundary element methods. However, this work also assumed prescribed mode shapes for the structure, rather than attacking the fully coupled FSI problem. In a very recent investigation, Shen et al. [37] explored viscous fluid nonlocality in the context of flexural vibrations of a cantilever plate in cylindrical bending. In this important contribution, the hydrodynamic problem is solved analytically and a hydrodynamic function is derived for use in the structural problem. However, the remarkable method is based on the strong assumption of solid deformations independent of the chord coordinate. The validity of this assumption for complex plate-like vibrations was not fully investigated. In particular, one immediate limitation of the theory is the absent treatment of torsional (or more complex plate-like) modes that are inherently dependent of the chord coordinate of the structure. As such, investigation of complex but realistic flexural-torsion scenarios and proper plate-modes are not within the scope of this work. This short review demonstrates that, despite the number of studies that shows the inadequacy of the local theory, and innovative attempts at addressing these shortcomings, to the best of the authors' knowledge, a comprehensive and fully coupled FSI 3D nonlocal theory for realistic vibrations is not yet available.

The objective of this paper is thus to develop a nonlocal 3D hydrodynamics theory for the strongly coupled FSI problem concerning the small amplitude vibrations of a submerged thin, light, flexible cantilevered structure in a heavy fluid. More specifically, we consider linear elastic plate-like solids undergoing geometrically linear deformations, in the limit of vanishingly small displacements and rotations. Thus we are concerned with hydrodynamics in the limit of zero Keulegan-Carpenter number, defined as $KC = 2\pi A_0/b$, where A_0 is a characteristic amplitude of oscillation and b is a characteristic transverse dimension of the solid [47, 48, 49]. As $KC \rightarrow 0$, the nonlinear convective term in the Navier-Stokes equations become negligible and the flow regime can be conveniently described by a frequency parameter, often indicated by $\beta = (\rho_f \omega b^2)/(2\pi \mu_f)$, see also [50], where ω is the oscillation radian frequency and ρ_f and μ_f are the fluid's density and dynamic viscosity. In this hydrodynamic regime, often denoted as the unsteady Stokes regime [51], the conventionally defined Reynolds number, based on a characteristic velocity ωA_0 , can be expressed as the product β KC and tends to 0. Within these hypotheses and in these ranges of validity, unique aspects of this contribution include: i) the seamless treatment of low aspect ratio structures for both beam and plate mechanics

in viscous fluids; ii) a rigorous 3D treatment of the fluid problem; iii) integration of the FSI theory in an "exact", fully coupled, computationally efficient formalism. In particular, our new method develops the new concept of the so-called complex-valued "nonlocal modal hydrodynamic function matrix" to formalize the two-way coupling between the structural mechanics and the fluid dynamics.

The general overview of our method is as follows. First, the structural dynamics for classical plates and beams is treated in a semi-analytical fashion, via Rayleigh-Ritz discretization of the energy functionals into lumped parameter equations of motion, written in a basis of admissible in vacuo modes for the structure. The hydrodynamic load is introduced in the equations of motion as a nonlocal function of the structure vibration, via the definition a hydrodynamic operator to be identified. A semi-analytical FSI treatment based on the oscillatory Stokeslet theory is used to construct a representation of the hydrodynamic operator on the same basis of admissible modes. Crucially, the FSI solution determines the distributed hydrodynamic loading resulting from the entire vibration characteristics of the cantilevered structure, and is therefore genuinely nonlocal and 3D. This representation takes the form of the nonlocal modal hydrodynamic function matrix that is then incorporated in the structural mechanics model. The two way coupling of the problem allows to calculate the vibration response of the system to an external excitation, as well as the resulting fluid flow field. Notably, neither of these quantities are specified a priori, but they both are the result of the fully coupled FSI solution.

Once our novel theory is developed, we explore the nature of the nonlocal hydrodynamic operator and its implications on the coupling of otherwise orthogonal structural modes through both inertial and damping fluid loading. Specifically, even in an orthogonal basis, the representation of the hydrodynamic operator is non diagonal, in a stark departure from the local hydrodynamics approaches. By appeal to an energy argument, we highlight a novel "reciprocity" result, reflected in the symmetry properties of the hydrodynamic operator, as well as a parity preserving property. We demonstrate the characteristics of our novel theory by studying frequency response functions (FRFs), mode shapes in vacuo ("dry") and in the viscous fluid ("wet"), hydrodynamic forces and their components in phase with acceleration or velocity of the structure (respectively, added mass and damping effects), quality factors and added mass ratio coefficients and compare them with the predictions of the local theory for both beam and plate analysis. We further investigate the effect of the fluid on the vibrational shapes at resonance and support our conclusions via detailed studies of the flow fields corresponding to selected vibration cases. Importantly, we verify our nonlocal plate theory with a new set of experiments for a square plate under base excitation demonstrating striking agreement and predictive capabilities.

Within our working hypotheses, our approach establishes an "exact" solution, since the FSI problem is constructed in full 3D generality with only the assumption of thin cantilever. Therefore, the effect of boundary conditions, finite aspect ratio, and nonlocality are naturally captured by the method. Importantly, the FSI problem is solved "offline" for a desired combination of geometry and dynamic parameters. As a result, our coupled method is computationally inexpensive, while retaining its exact semi-analytical nature. In fact, the only approximations in our method consist in the numerical discretization and can be controlled as desired, albeit at the cost of increase computational cost.

The rest of the paper is organized as follows. In Sec. 2, we establish the fundamental framework of our method, including how the nonlocal modal hydrodynamic matrix is incorporated in vibrational models of both cantilever beams and plates. In Sec. 3, we present the solution of the hydrodynamic problem, defining explicitly the nonlocal modal hydrodynamic matrix, and highlighting important aspects of the fluid response. In Sec. 4, we discuss the construction of the fully coupled FSI model, with particular interest to the integration of the nonlocal hydrodynamics in the structural model. In Sec. 5, we present a through investigation of underwater vibrations of beams and plates, including theoretical, numerical, and experimental contributions. Conclusions are summarized in Sec. 6. For ease of presentation, we provide tutorial-like material on classical mechanics of beams and plates, as well as results on singularities for the solution of hydrodynamic problems and their asymptotics in the Appendices.

2. Governing equations of motion

In this section, we will develop the general framework of equations of motion including the nonlocal modal hydrodynamic function matrix formalism which is, in principle, applicable to any solid structure vibrating in viscous fluids. As we focus on vibrations of both cantilever plate and beam geometries, we consider here a plate-like solid, submerged in the fluid, undergoing small deflections in the transverse direction. The undeformed plate mid-plane lies in the *xy*-plane, and its length, width, and thickness lie along the *x*, *y*, and *z* axes of the reference frame, respectively.

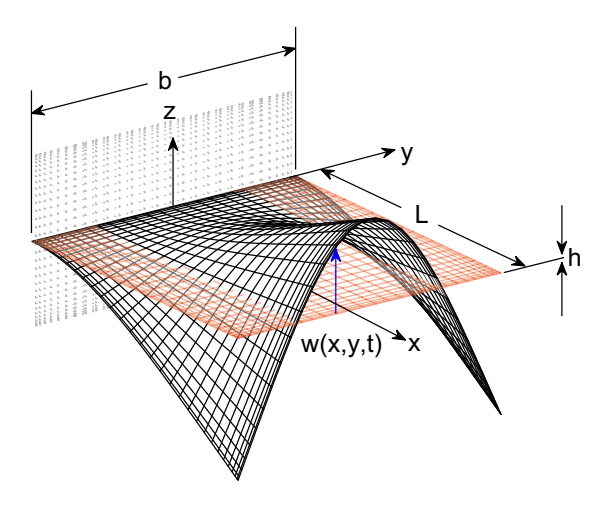


Figure 1: Geometry and nomenclature of the problem. The instantaneous displacement of the structure, undergoing complex plate-like vibrations, are exaggerated for clarity of presentation.

The origin of the reference frame is placed at the centroid of the fixed-end cross section at x = 0. Length, width, and thickness of the plate are denoted as L, b, and h, respectively. The fixed edge is at x = 0, and the free edges are at x = L and $y = \pm b/2$. The assumption throughout this work is that $h \ll b$, so that we will consider the solid as a mathematical surface, with zero thickness, whose reference configuration is given by the domain $D = \{(x, y, z) \in \mathbb{R}^3 | x \in [0, L], y \in [-b/2, b/2], z = 0\}$. The geometry and nomenclature of the problem are presented in Fig. 1.

We will consider throughout small displacements and rotations for the structure, which thus behaves as a linear elastic solid, and linear hydrodynamic response for the fluid, which operates linearly in the unsteady Stokes regime. Because of this hypothesis, the current configuration of the solid also coincides with the reference configuration. We will also postulate that the solid material is homogeneous and isotropic. We will further focus on steady state harmonic vibrations, which exist under the above hypotheses, either in a free vibration problem or in a harmonically-forced problem.

2.1. Definition of the structural problem

Let us denote with w(x, y, t) the transverse displacement in the z-direction of any point in the structure, labeled via its Cartesian coordinates $\mathbf{x} = (x, y)$. Here and elsewhere, t indicates the time variable. For a linear harmonic vibration at the radian frequency ω , it is convenient to replace the physical displacement with its phasor $\hat{w}(\mathbf{x})$, such that $w(x, y, t) = \text{Im}\left[\hat{w}(\mathbf{x})e^{i\omega t}\right]$ with $i = \sqrt{-1}$, see for example [29]. Here and in the following, a superimposed hat indicates phasor quantities.

Typical equations of motion in vacuo are generally written, in the frequency domain, as $-\omega^2 \mathcal{M}[\hat{w}(x)] + \mathcal{K}[\hat{w}(x)] = \hat{\mathcal{F}}_{\text{ext}}(x)$, where \mathcal{M} and \mathcal{K} indicate some linear operators describing the inertia and stiffness behavior of the structure, respectively, and $\hat{\mathcal{F}}_{\text{ext}}(x)$ describes the phasor of a possibly non-zero distributed harmonic forcing term. This equation is supplemented by a suitable set of boundary conditions that, in the case of a cantilevered structure, includes free edges except one fixed edge. Initial conditions are not necessary in the phasor problem, as we focus on the steady state vibrational behavior, after all transients have decayed, see [29].

To incorporate the effect of the encompassing fluid on the vibrations of the cantilever, we modify this equation of motion by including a term describing the steady-state hydrodynamic force per unit area on the structure, arising from the fluid-structure interactions. This force is generated by the structure vibrating with a shape $\hat{w}(x)$ at a frequency ω , or equivalently with a velocity $i\omega\hat{w}(x)$. To emphasize both these points, we indicate this force with the symbol $\mathcal{H}_{\omega}[\hat{w}(x)]$. In practice, this force is given by the net traction across the structure, projected in the direction normal to the solid surface, see for example [46]. It is important to remark here that $\mathcal{H}_{\omega}[\hat{w}(x)]$ provides, at every point in the domain D, the hydrodynamic forces generated by the motion of the entire structure, at a particular oscillation frequency. It is known that this force, in the unsteady Stokes problem, is a linear operator on the shape $\hat{w}(x)$, and is harmonic at the frequency ω , but in general is a nonlocal complex function of the entire velocity of the structure [51, 46].

Under these hypotheses, the equations of motion for the solid in the frequency domain become

$$-\omega^2 \mathcal{M}[\hat{w}(\mathbf{x})] + \mathcal{K}[\hat{w}(\mathbf{x})] = \hat{\mathcal{F}}_{\text{ext}}(\mathbf{x}) + \mathcal{H}_{\omega}[\hat{w}(\mathbf{x})]$$
 (1)

Here, the right hand side (beside the external forcing term) is novel and represents the still-undetermined, frequency domain description of the point-wise hydrodynamic forces on the structure due to oscillation of the entire structure at a specific frequency ω . The unique aspect of this approach is that the motion of the entire structure is taken into account for the calculation of the hydrodynamic forces, thus naturally capturing edge effects and FSI singularities that are normally neglected by local approaches such as those based on [22, 1]. In addition, no prescription on the deformed shape of the cantilever or on the particular mode of vibration is necessary at this point. This constitutes an important generalization from [46], in which the vibration was instead prescribed along a specific deformed shape, and from [37], in which the vibration was instead prescribed along structural beam modes (cylindrical bending). It also represents an altogether different approach from [35], in which prescribed chord-wise deformations are necessary to calculate the hydrodynamic response in a strip-like, still local, method. As detailed later, these effects are important especially in the case of relatively low aspect ratio cantilevers and for higher modes of vibration, and they are essential for evaluation of the plate behavior.

2.2. Discretization

For the solution of the structural problem in Eq. (1), we will use a form of the Rayleigh-Ritz energy method [39] to recast the linear problem in a finite-dimensional matrix formulation. Relevant details are provided in the Appendix on how the structural matrices are derived from expressions of the energy functionals. Here, however, to illustrate the procedure and derive the modal hydrodynamic function matrix, we will use the somewhat more familiar Galerkin method, see for example [52], which instead uses Eq. (1) directly. Specifically, we assume that the phasor $\hat{w}(x)$ can be generally represented as a superposition of "modes" (actual or assumed) modulated by frequency dependent modal amplitudes, that is, $\hat{w}(x) = \sum_j \hat{q}_j(\omega)\phi_j(x)$.

Once a suitable representation of $\hat{w}(x)$ is developed as a linear combination of admissible functions, by linearity, Eq. (1) becomes

$$-\omega^2 \sum_{j} \mathcal{M}[\phi_j(\mathbf{x})] \hat{q}_j(\omega) + \sum_{j} \mathcal{K}[\phi_j(\mathbf{x})] \hat{q}_j(\omega) = \hat{\mathcal{F}}_{\text{ext}}(\mathbf{x}) + \sum_{j} \mathcal{H}_{\omega}[\phi_j(\mathbf{x})] \hat{q}_j(\omega)$$
(2)

Provided that the chosen modes constitute a complete basis for the space of square-integrable functions over D, "projection" of Eq. (2) on the modes $\phi_i(x)$ yields a set of linear algebraic equations for the modal amplitudes $\hat{q}_j(\omega)$ in the form

$$-\omega^{2} \sum_{j} \int_{D} \phi_{i}(\mathbf{x}) \mathcal{M}[\phi_{j}(\mathbf{x})] d\mathbf{x} \, \hat{q}_{j}(\omega) + \sum_{j} \int_{D} \phi_{i}(\mathbf{x}) \mathcal{K}[\phi_{j}(\mathbf{x})] d\mathbf{x} \, \hat{q}_{j}(\omega) =$$

$$\int_{D} \phi_{i}(\mathbf{x}) \hat{\mathcal{F}}_{\text{ext}}(\mathbf{x}) d\mathbf{x} + \sum_{j} \int_{D} \phi_{i}(\mathbf{x}) \mathcal{H}_{\omega}[\phi_{j}(\mathbf{x})] d\mathbf{x} \, \hat{q}_{j}(\omega) \quad (3)$$

or, with obvious meaning of the symbols,

$$-\omega^2 \sum_{j} m_{ij} \hat{q}_j(\omega) + \sum_{j} k_{ij} \hat{q}_j(\omega) = \hat{f}_i(\omega) + \sum_{j} h_{ij}(\omega) \hat{q}_j(\omega)$$
 (4)

where $m_{ij} = \int_{D} \phi_i(\mathbf{x}) \mathcal{M}[\phi_j(\mathbf{x})] d\mathbf{x}$ and $k_{ij} = \int_{D} \phi_i(\mathbf{x}) \mathcal{K}[\phi_j(\mathbf{x})] d\mathbf{x}$ are the usual modal mass and stiffness terms found in structural matrices $[\mathbf{M}]_{ij} = m_{ij}$ and $[\mathbf{K}]_{ij} = k_{ij}$, and $\hat{f}_i(\omega) = \int_{D} \phi_i(\mathbf{x}) \hat{\mathcal{F}}_{\text{ext}}(\mathbf{x}) d\mathbf{x}$ is the *i*-th component of the modal

¹In the Galerkin method, the modes are chosen to satisfy all the (homogeneous form of the) boundary conditions of the problem [52, 53]. By contrast, the practical advantage of the Rayleigh-Ritz method lies in the use of assumed modes that only need to satisfy the essential boundary conditions and that the discretization into the matrix problem is performed from expressions for the energy of the system [52].

external excitation vector \hat{f} . These structural terms are fully detailed in the Appendix for the beam and plate theories, separately, although derived from energy methods. Importantly, in Eq. (4), we have explicitly defined the term

$$[\boldsymbol{H}(\omega)]_{ij} = h_{ij}(\omega) = \int_{\boldsymbol{D}} \phi_i(\boldsymbol{x}) \mathcal{H}_{\omega}[\phi_j(\boldsymbol{x})] d\boldsymbol{x}$$
 (5)

which represents the hydrodynamic force generated by the structure vibrating in the fluid along the structural mode ϕ_j at a frequency ω , projected on the mode ϕ_i . We define this new quantity as the ij-entry of the nonlocal modal hydrodynamic function matrix. An insightful interpretation of Eq. (5) is that the frequency-dependent linear operator $\mathcal{H}_{\omega}[\bullet]$ is being fully characterized by determining its components in the "coordinate system" established by a complete set of basis vectors, in this case constructed from the structural modes. The determination of the matrix $\mathbf{H}(\omega)$ and an investigation of its physical properties is central to this paper and will be addressed in Sec. 3 via solution of the hydrodynamic problem.

2.3. Treatment of base acceleration excitation

A subtle manifestation of nonlocal hydrodynamics also appears in the practical cases of structures excited by an imposed base acceleration rather than an external force, see for example [29, 54]. In this case, let us denote with $W_B(x, y, t) = \text{Im} \left[\hat{W}_B e^{i\omega t} \right]$ the rigid translational displacement of the base, where \hat{W}_B is the complex amplitude of the rigid base displacement, uniform over the domain D. Also, we denote with $\Theta_B(x, y, t) = \text{Im} \left[\hat{\Theta}_B e^{i\omega t} \right]$ the rigid rotation angle of the base, with $\hat{\Theta}_B$ the complex amplitude of the rigid base rotation, uniform over the domain D. The absolute motion of the cantilever will thus be $w(x, y, t) + W_B(x, y, t) + y\Theta_B(x, y, t)$ and this term appears in the inertial operator \mathcal{M} and in the hydrodynamic force operator \mathcal{H}_{ω} . Because of the linearity of the operators, we have

$$\hat{\mathcal{F}}_{\text{ext}}(\mathbf{x}) = \hat{W}_B \omega^2 \mathcal{M}[\mathbf{1}(\mathbf{x})] + \hat{\Theta}_B \omega^2 \mathcal{M}[y\mathbf{1}(\mathbf{x})] + \{\hat{W}_B \mathcal{H}_{\omega}[\mathbf{1}(\mathbf{x})] + \hat{\Theta}_B \mathcal{H}_{\omega}[y\mathbf{1}(\mathbf{x})]\}$$
(6)

where we have used the symbol $\mathbf{1}(x)$ to indicate the function identically equal to 1 on the domain D and 0 otherwise. The first two terms on the right hand side are the familiar base acceleration excitation (in vacuo), while the term in braces includes the effect of the fluid. This expression can be used seamlessly in Eq. (3) for the calculation of the modal forces. We conclude by observing that, in case of base acceleration excitation, the hydrodynamic load on the cantilever will comprise both the component due to the elastic deformation of the solid, that is, $\sum_j \mathcal{H}_{\omega}[\phi_j(x)]\hat{q}_j(\omega)$, as well as that due to the rigid body motion $\hat{W}_B\mathcal{H}_{\omega}[\mathbf{1}(x)]$ and $\hat{\Theta}_B\mathcal{H}_{\omega}[y\mathbf{1}(x)]$. In particular, this nonlocal term in the structural excitation has not been identified before in the context of hydrodynamic function approaches. This has important consequences in the dynamic response of the system excited by a base acceleration, rather than by an applied external force, as discussed in the study of experimental results in Sec. 5.

3. The hydrodynamic problem

3.1. Problem statement and solution

We consider here a prototype cantilevered thin structure and thus continue to focus on a 2D thin sheet. Geometry and nomenclature are as in Fig. 1. We remark here that the x-direction is span-wise and the y-direction is chord-wise. As above, the thickness h of the cantilever is assumed to be much smaller of either length and width and will be neglected in the hydrodynamic calculations, thus considering the cantilever as a zero thickness sheet. The structure is submerged in a quiescent viscous fluid of density ρ_f and dynamic viscosity μ_f .

The hydrodynamic regime of interest is described by the unsteady Stokes equations, for which convective non-linearities are neglected [46]. The flow is assumed to be incompressible and in absence of gravity and body forces. Steady-state vibrations of the cantilevered structure are assumed to be harmonic and to occur at vanishingly small amplitude. Under these assumptions, the evolution of the fluid velocity field is also time-harmonic. By nondimensionalizing all variables with the characteristic length b, the characteristic velocity ωb , and the dynamic viscosity μ_f , the nondimensional velocity phasor \hat{u} is given by the following equation in the frequency domain [51]

$$i\alpha^2 \hat{\boldsymbol{u}} = -\boldsymbol{\nabla}\hat{\boldsymbol{p}} + \nabla^2 \hat{\boldsymbol{u}} \tag{7}$$

in addition to the incompressibility condition $\nabla \cdot \hat{\boldsymbol{u}} = 0$, where $\alpha^2 = \omega \rho_f b^2/\mu_f = 2\pi\beta$. Here, \hat{p} indicates the nondimensional pressure phasor, obtained from the dimensional pressure scaled by the characteristic pressure $p_0 = \mu_f \omega$, resulting from the nondimensionalization. Furthermore, the parameter α^2 , proportional to the nondimensional frequency parameter β , can be understood as the ratio [55] of the Reynolds number versus the Strouhal number for this problem. All phasors in Eq. (7) are functions of the spatial location and of the frequency ω , but we omit here this dependency for brevity. No-slip boundary conditions are imposed at the fluid-solid interface \boldsymbol{D} , that is, the cantilever surface. Remote boundary conditions at infinity include zero pressure and zero velocity [46].

The solution of Eq. (7) can be written as in [51, 46], in terms of the following Fredholm integral equation of the first kind in index notation (indices i, j, k = 1, 2, 3)

$$\hat{u}_i(\bar{\mathbf{x}}) = \frac{1}{8\pi} \int_D \hat{\tau}_{jk}(\mathbf{x}) n_k S_{ij}(\mathbf{x}, \bar{\mathbf{x}}; \alpha) \, d\mathbf{x}$$
 (8)

which for simplicity is already collocated on the fluid-solid interface. Here, x and \bar{x} are any two points on the cantilever surface, n_k is the normal unit vector to the surface of the cantilever, $\hat{\tau}_{jk}$ is the phasor of the (nondimensional) stress tensor, and S_{ij} is the oscillatory Stokeslet defined in [51], see also Appendix C.1. The dimensional stress tensor is recovered from $\hat{\tau}_{jk}$ by multiplication with p_0 . The physical meaning of Eq. (8) is that a traction $\hat{\tau} \cdot n$ at x induces a velocity field \hat{u} at \bar{x} . In essence, we will solve Eq. (8) for the stress state on the cantilever (which will provide the hydrodynamic forcing) as a function of its vibrational velocity.

Rather than developing Eq. (8) in its full generality, here we discuss a simplified treatment for the specific case of interest. The first simplification, as in [46], is the assumption of zero thickness cantilever. This allows for neglecting the contributions of the stress on the sides of the cantilever parallel to the zx- and zy-planes. The second assumption is that of linearized out-of-plane displacements for the structure, described by the phasor \hat{w} . This implies that the fluid velocities along the x- and y-axes vanish at the surface of the cantilever, and that the nondimensional velocity phasor $\hat{u}(x) = i\omega \hat{w}(x)e_3/(\omega b)$ for $x \in D$, where e_3 is the unit vector in the z-direction. By linearity, the only non-zero component of stress is $\hat{\tau}_{33}$. Thus, by denoting with $[[\hat{\tau}]] = n_3(\hat{\tau}_{33}|_{z=0^+} - \hat{\tau}_{33}|_{z=0^-})$ the jump of the traction across D, we obtain the following single scalar integral equation

$$i\hat{w}(\bar{\mathbf{x}})/b = \frac{1}{8\pi} \int_{D} [[\hat{\tau}]](\mathbf{x}) \mathcal{A}(|\mathbf{x} - \bar{\mathbf{x}}|, \alpha) \, d\mathbf{x}$$
(9)

which shows that $[[\hat{\tau}]]$ depends linearly on the phasor of the transverse nondimensional velocity $i\hat{w}/b$ through the kernel \mathcal{A} . By indicating with $r = |x - \bar{x}|$ the distance of two points x and \bar{x} on the cantilever, the kernel was shown in [46] to reduce to

$$\mathcal{A}(r,\alpha) = 2\frac{e^{-\sqrt{i}\alpha r}}{r} \left(1 + \frac{1}{\sqrt{i}\alpha r} - \frac{i}{\alpha^2 r^2} \right) + \frac{2i}{\alpha^2 r^3}$$
 (10)

It is useful to note that the kernel \mathcal{A} is invariant with respect to any transformation that preserves the distance between x and \bar{x} . In particular, \mathcal{A} is invariant if both x and \bar{x} are reflected about the y-axis. This observation has important implications on the odd or even nature of the hydrodynamic load in correspondence to an odd or even velocity profile about the y-axis and can be used in practical calculations. We call this a parity-preserving property.

Equation (9) can be solved numerically for $[[\hat{\tau}]]$ for any specific form of out-of-plane displacement \hat{w} and frequency ω (or parameter α) with the methods discussed in detail in [46] using boundary integrals and variations of the panel method. Further details can be found in Appendix C.2. It is of particular interest to solve for $[[\hat{\tau}]]$ in correspondence of $\hat{w}(x)$ replaced with one "mode" (either actual or assumed) for the structure, say $\phi_i(x)$. Recognizing in fact that $\mathcal{H}_{\omega}[\hat{w}] = [[\hat{\tau}]]$, in this case, the net traction takes on the meaning of the generic term $\mathcal{H}_{\omega}[\phi_i(x)]$ that was introduced in Eq. (2). The solution will thus correspond to the phasor of the nondimensional hydrodynamic force per unit area due to fluid-structure interactions occurring for vibrations along the *i*-th mode at a frequency ω . We will indicate this quantity with $\hat{\eta}_{\phi_i}(x,\omega) = \mathcal{H}_{\omega}[\phi_i(x)]$. This construction can be interpreted intuitively by thinking of the operator \mathcal{H}_{ω} as the inverse of the integral operator in Eq. (9), besides some scaling coefficient. At this stage, since the mechanical properties of the structure have not been specified, ω should be regarded as a free parameter.

In passing, we note that Eq. (8) can also be used to reconstruct the full 3D velocity field of the fluid in response to a net traction [[τ]] on the plate. For this purpose, the full expressions for the kernels S_{13} , S_{23} , and S_{33} are adapted from [51] and presented in Appendix C.1, along with expressions for the evaluation of the components of the vorticity vector.

3.2. The nonlocal modal hydrodynamic function matrix

Once the tools from the hydrodynamic treatment are available, we are now in the position of explicitly deriving the nonlocal modal hydrodynamic function matrix whose terms are defined in Eq. (5). To this aim, we will first produce an energy argument leading to a novel reciprocity result which has both interesting physical significance as well as usefulness in numerical calculations.

Recall that we have denoted with $\hat{\eta}_{\phi_i}$ the nondimensional forces corresponding, through Eq. (9), to the nondimensional velocities $\mathrm{i}\phi_i/b$. Switching now to dimensional quantities, let us consider an experiment in which fluid forces $\mu_f\omega\hat{\eta}_{\phi_i}$ are applied to the structure to generate a velocity field $\mathrm{i}\omega\phi_i$. Then, on top of the existing load distribution, a second set of fluid forces $\mu_f\omega\hat{\eta}_{\phi_j}$ are applied to the structure to generate an additional velocity field $\mathrm{i}\omega\phi_j$. Obviously, because of linearity, the total distribution of forces on the structure is $\mu_f\omega(\hat{\eta}_{\phi_i}+\hat{\eta}_{\phi_j})$ and the total velocity distribution is $\mathrm{i}\omega(\phi_i+\phi_j)$. Here, without loss of generality, ϕ_i and ϕ_j are assumed to be real, as the only requirement in a virtual work argument is that the displacements are admissible. For the load sequence above, the (complex) work done by the hydrodynamic forces on the structure is

$$\mathcal{W}_{H,i\to j} = \mu_f \omega^2 \left(\frac{1}{2} \int_{D} [\mathrm{i}\phi_i(\mathbf{x})]^* \hat{\eta}_{\phi_i}(\mathbf{x},\omega) \mathrm{d}\mathbf{x} + \int_{D} [\mathrm{i}\phi_i(\mathbf{x})]^* \hat{\eta}_{\phi_j}(\mathbf{x},\omega) \mathrm{d}\mathbf{x} + \frac{1}{2} \int_{D} [\mathrm{i}\phi_j(\mathbf{x})]^* \hat{\eta}_{\phi_j}(\mathbf{x},\omega) \mathrm{d}\mathbf{x} \right)$$
(11)

where the superscript star indicates complex conjugation. Note that, while the work contributions including the product of ϕ_i with $\hat{\eta}_{\phi_i}$ and ϕ_j with $\hat{\eta}_{\phi_j}$ are premultiplied by a factor 1/2 because force and velocity increase proportionally, the mixed term including the product of ϕ_i with $\hat{\eta}_{\phi_j}$ is not, because the new force $\hat{\eta}_{\phi_j}$ does work on the full value of the velocity $i\phi_i$. Reversing the order of application of the forces, we obtain the complex work done in this opposite sequence as

$$\mathcal{W}_{H,j\to i} = \mu_f \omega^2 \left(\frac{1}{2} \int_D [\mathrm{i}\phi_j(\mathbf{x})]^* \hat{\eta}_{\phi_j}(\mathbf{x},\omega) \mathrm{d}\mathbf{x} + \int_D [\mathrm{i}\phi_j(\mathbf{x})]^* \hat{\eta}_{\phi_i}(\mathbf{x},\omega) \mathrm{d}\mathbf{x} + \frac{1}{2} \int_D [\mathrm{i}\phi_i(\mathbf{x})]^* \hat{\eta}_{\phi_i}(\mathbf{x},\omega) \mathrm{d}\mathbf{x} \right)$$
(12)

Because it must be that $W_{H,i\to j} = W_{H,j\to i}$ for conservation of energy, and noting that the modes ϕ_i are real, we obtain the important result

$$\int_{D} \phi_{i}(\mathbf{x}) \hat{\eta}_{\phi_{j}}(\mathbf{x}, \omega) d\mathbf{x} = \int_{D} \phi_{i}(\mathbf{x}) \mathcal{H}_{\omega}[\phi_{j}(\mathbf{x})] d\mathbf{x} = \int_{D} \phi_{j}(\mathbf{x}) \hat{\eta}_{\phi_{i}}(\mathbf{x}, \omega) d\mathbf{x} = \int_{D} \phi_{j}(\mathbf{x}) \mathcal{H}_{\omega}[\phi_{i}(\mathbf{x})] d\mathbf{x}$$
(13)

or $h_{ii}(\omega) = h_{ii}(\omega)$ as, through this argument, we have naturally recovered the terms in Eq. (5). Equation (13) could be called a "reciprocity result", similar to the Maxwell-Betti theorem, in this FSI problem. More specifically, this establishes the real and imaginary parts of the matrix $H(\omega)$ as symmetric, that is $\text{Re}[H(\omega)] = \text{Re}[H(\omega)]^T$ and Im $[H(\omega)] = \text{Im} [H(\omega)]^T$. The matrix $H(\omega)$ however is not Hermitian, that is, $H(\omega)$ is not equal to its complexconjugate transpose. If that were the case, the imaginary part of $H(\omega)$ would be a skew matrix and describe gyroscopic effects [56] rather than dissipation, see also [57]. Physically, this relation demonstrates also that the hydrodynamic force generated in response to vibration along mode j does work on a velocity field along mode i equal to the work of the hydrodynamic force generated in response to vibration along mode i on a velocity field along mode j. In a different interpretation, referring back to Eq. (3), this relation demonstrates that the i-th modal hydrodynamic force generated in response to vibration along mode j is equal to the j-th modal hydrodynamic force generated in response to vibration along mode i. Computationally, this result can reduce approximately by half the cost of calculating $H(\omega)$, as well as providing a built-in consistency check in the numerics. As expected, this reciprocity is invariably observed in the numerical calculations. Furthermore, by considering the fluid kinetic energy and viscous dissipation, we deduce that both Re $[H(\omega)]$ and $-\text{Im}[H(\omega)]$ must be positive definite, a circumstance that is consistently observed in the numerical results. Note that the prescribed boundary conditions do not allow the fluid matrices to be positive semidefinite, see also [57].

With the reciprocity result, the dimensional nonlocal modal hydrodynamic function matrix components for both plate and beam cantilever structures to be used in a suitable structural dynamics model can be determined as follows. Rewriting slightly for clarity, for plates we have

$$h_{ij}(\omega) = \mu_f \omega \int_0^L \int_{-b/2}^{b/2} \phi_i(\mathbf{x}) \hat{\eta}_{\phi_j}(\mathbf{x}, \omega) dy dx = \mu_f \omega \int_0^L \int_{-b/2}^{b/2} \phi_j(\mathbf{x}) \hat{\eta}_{\phi_i}(\mathbf{x}, \omega) dy dx = h_{ji}(\omega)$$
(14)

where we have used the symmetry properties of Eq. (13). A natural interpretation of this expression derives from recognizing the projection of $\hat{\eta}_{\phi_j}(\mathbf{x}, \omega)$ onto $\phi_i(\mathbf{x})$ or, equivalently, of $\hat{\eta}_{\phi_i}(\mathbf{x}, \omega)$ onto $\phi_j(\mathbf{x})$ because of reciprocity, via an inner product (double integral over $\mathbf{D} = [0, L] \times [-b/2, b/2]$) over a suitable function space, see also Eq. (3). Because of the parity-preserving property, it is interesting to note that if the mode ϕ_i is an even (odd) function of y, the corresponding hydrodynamic load $\hat{\eta}_{\phi_i}$ will be even (odd) as well, as shown in Fig. 2. Then, if a second ϕ_j is odd (even), the term h_{ij} will evaluate to 0. This property, consistent with physical intuition, stems from the invariance of the kernel \mathcal{A} and explains the presence of sparsity patterns in the matrix \mathbf{H} for plates.

Vice versa, for beams in bending, as the modes (but not the hydrodynamic loads) are only function of x, Eq. (14) can be rewritten in the slightly modified form

$$h_{ij}(\omega) = \mu_f \omega \int_0^L \phi_i(x) \left(\int_{-b/2}^{b/2} \hat{\eta}_{\phi_j}(\boldsymbol{x}, \omega) dy \right) dx = \mu_f \omega \int_0^L \phi_j(x) \left(\int_{-b/2}^{b/2} \hat{\eta}_{\phi_i}(\boldsymbol{x}, \omega) dy \right) dx$$
(15)

which is computationally equivalent to Eq. (14) but helps better identifying the force per unit length $\int_{-b/2}^{b/2} \hat{\eta}_{\phi_j}(\mathbf{x},\omega) \mathrm{d}y$ that appears naturally in a one-dimensional (1D) beam problem. A similar form was proposed in a previous work by our group [46] for a prescribed mode shape. Equation (15) can be recognized as the projection of the hydrodynamic force per unit length $\int_{-b/2}^{b/2} \hat{\eta}_{\phi_j}(\mathbf{x},\omega) \mathrm{d}y$ onto the beam mode $\phi_i(x)$ via an inner product (integral over $x \in [0,L]$). This development shows that the modal hydrodynamic function matrix for beams in bending can be thought of a subset of that for plates as only modes independent of y are used for the beam case. In this respect, the limitations of the bending beam formulation are somewhat reminiscent to those of the recent work of [37]. Note that, since all modes and hydrodynamic loads per unit length are independent of y, no even or odd patterns occur, and the sparsity patterns are not observed in the beam case.

Following the literature, it is convenient to express the hydrodynamic function in terms of the nondimensional frequency parameter β . Therefore, the modal hydrodynamic function terms are scaled as

$$\tilde{h}_{ij}(\beta) = \left. \frac{h_{ij}(\omega)}{(\pi/4)\rho_f \omega^2 b^2 L} \right|_{\omega = (2\pi\mu_f \beta)/(\rho_f b^2)} \tag{16}$$

This position makes $\tilde{h}_{ij}(\beta)$ independent of the specific dimensional parameters of the problem and reduces it to a function of aspect ratio $\Lambda = L/b$ and nondimensional frequency parameter β , provided that the fluid characteristics (ρ_f, μ_f) and the cantilever width b (normally taken to unity in the hydrodynamic calculations) are prescribed. Notice, in fact, that the scaling coefficient in Eq. (16) equates to $(\pi/4)\rho_f\omega^2b^2L = [(\pi^3\mu_f^2)/(\rho_fb)]\Lambda\beta^2$.

4. Construction of the fully coupled FSI model

4.1. Nonlocal hydrodynamic coupling as added mass and damping matrices

Once the matrix $H(\omega)$ is known, the dynamic behavior of the system can be determined by solving the fully coupled FSI problem in Eq. (4). For example, the free vibration problem with $\hat{f} = \mathbf{0}$ leads to a special form of the generalized eigenvalue problem written as

$$[K - \omega^2 M - H(\omega)]\hat{\mathbf{q}}(\omega) = \mathbf{0}$$
(17)

where $\hat{q}(\omega)$ is the vector of modal coefficients. Because $H(\omega)$ is a complex-valued function of ω , it is illustrative to write $H(\omega) = \omega^2 H_R(\omega) - i\omega H_I(\omega)$ to isolate its real and imaginary parts and recast Eq. (17) as $[K - \omega^2(M + H_R(\omega)) + i\omega H_I(\omega)]\hat{q}(\omega) = 0$. Note that, for reciprocity as in Eq. (13), $H_R(\omega) = H_R(\omega)^T$, and $H_I(\omega) = H_I(\omega)^T$. With this construction, it becomes apparent that the real part of the modal hydrodynamic function matrix behaves as an added mass matrix, while its imaginary part behaves as a damping matrix, or energy dissipation, term [28]. They are correctly described via symmetric and positive definite matrices, for any ω . Both effects are, however, frequency dependent, so that Eq. (17) represents a so-called nonlinear eigenvalue problem [58], whose solution is nontrivial and requires special approaches.²

²Analysis of Eq. (17) could be pursued numerically by scanning for eigenfrequencies and modes as a function of ω by monitoring the magnitude of the vector \hat{q} or the behavior of the determinant (or, more accurately, the condition number or singular values) of the matrix in square brackets in Eq. (17).

In this work, we will not be concerned with the solution of the nonlinear eigenvalue problem, but we choose to study the fully coupled FSI problem by investigating forced vibration scenarios. We will focus on solutions of $[K - \omega^2 M - H(\omega)]\hat{q}(\omega) = \hat{f}(\omega)$ and look for resonance peaks in the system FRF, for different relevant cases of external excitation.

4.2. Flexural vibrations of submerged cantilever beams

In this section, we specialize our previous results to cantilever beams undergoing bending vibrations. A review of the relevant foundational aspects of mechanics of beam vibrations is covered in Appendix A, along with a primer on our mechanical model. For an arbitrary external modal excitation, Eq. (4), in which the hydrodynamic force expressions in Eq. (15) are employed along with the structural matrices of Eq. (A.5) developed in the Appendix, is rewritten as

$$\left[EIL\tilde{\mathbf{K}} - \omega^2 \rho_s A L\tilde{\mathbf{M}} - \frac{\pi}{4} \rho_f \omega^2 b^2 L\tilde{\mathbf{H}}(\omega)\right] \hat{\mathbf{q}}(\omega) = \hat{\mathbf{f}}(\omega)$$
(18)

For illustration purposes, it is instructive to rewrite this expression as

$$\left[\tilde{\mathbf{K}} - \omega^2 \frac{\rho_s A}{EI} \tilde{\mathbf{M}} [\mathbf{I} + \mathcal{R} \tilde{\mathbf{M}}^{-1} \tilde{\mathbf{H}} (\omega)]\right] \hat{\mathbf{q}}(\omega) = \frac{1}{EIL} \hat{\mathbf{f}}(\omega)$$
(19)

where I is the identity matrix, and we defined $\mathcal{R} = (\pi \rho_f b)/(4\rho_s h)$ the mass ratio [29] of the FSI problem, which represents a measure of the amount of fluid loading that the structure is experiencing. This parameter can also be interpreted as the ratio of the mass per unit length of a cylinder of fluid of diameter b to the mass per unit length of the cantilever, see also [59]. In particular, if $\mathcal{R} \to 0$ the problem reduces to in vacuo vibrations, and for small values of \mathcal{R} the fluid only contributes to a small perturbation of the dynamics of the structure. Vice versa, the parameter \mathcal{R} becomes relatively large when light, flexible structures interact with dense fluids, that is, in the cases where the fluid significantly affects the dynamic behavior of the structure. Equation (19) bears formal similarities, as well as substantial differences, to the local theory, which reads, with the nomenclature of this paper,

$$\left[\tilde{\mathbf{K}} - \omega^2 \frac{\rho_s A}{EI} \tilde{\mathbf{M}} [1 + \Re \Gamma(\omega)]\right] \hat{\mathbf{q}}(\omega) = \frac{1}{EIL} \hat{\mathbf{f}}(\omega)$$
 (20)

Note here, that the classical hydrodynamic function $\Gamma(\omega)$ produced in [1] with the methods of [22] is a scalar function, rather than a matrix function as in Eq. (19). It is important to remark here that the off-diagonal terms of $H(\omega)$ are in general non-zero, even for a selection of orthogonal modes, due to the nonlocality of the operator. Importantly, modal coupling is not only inertial in nature, as typically observed [57], but also due to fluid damping. Even for a beam-like structure, this is a stark difference between our approach and the simplifying assumptions in the body of works inspired by [22, 1] which, by postulating that the hydrodynamic load per unit length is proportional to the local transverse acceleration of the beam axis, necessarily lead to a matrix H proportional, via a frequency-dependent complex scalar term, to the mass matrix M, and thus, diagonal for a choice of orthogonal modes.

4.3. Vibrations of submerged cantilever plates

In this section, we specialize our previous results to cantilever plates undergoing forced vibrations. A review of the relevant foundational aspects of mechanics of classical plate vibrations is covered in Appendix B, along with a primer on our mechanical model and its validation. Since our plate model can seamlessly capture flexural, torsional, and proper plate-like behavior of the structure, comparison of its predictions will also be discussed against bending and torsion results from beam models, as developed in Appendix A.³

For an arbitrary external modal excitation, the general expression in Eq. (4), in which the hydrodynamic force terms in Eq. (14) are employed along with the structural matrices of Eq. (B.5) developed in the Appendix, is rewritten as

$$\left[DLb\tilde{\mathbf{K}} - \omega^2 \rho_s h Lb\tilde{\mathbf{M}} - \frac{\pi}{4} \rho_f \omega^2 b^2 L\tilde{\mathbf{H}}(\omega)\right] \hat{\mathbf{q}}(\omega) = \hat{\mathbf{f}}(\omega)$$
 (21)

³For beams in torsion, similar to the problem discussed in [24, 54], several technical details make portions of the treatment somewhat different to what covered so far. For clarity of presentation, we will not introduce a nonlocal modal hydrodynamic theory for beams undergoing torsional vibrations in this work. The nonlocal torsional theory will be presented elsewhere. We will however compare predictions of torsional vibrations from our plate theory with the ad-hoc local torsional vibration theory of [24].

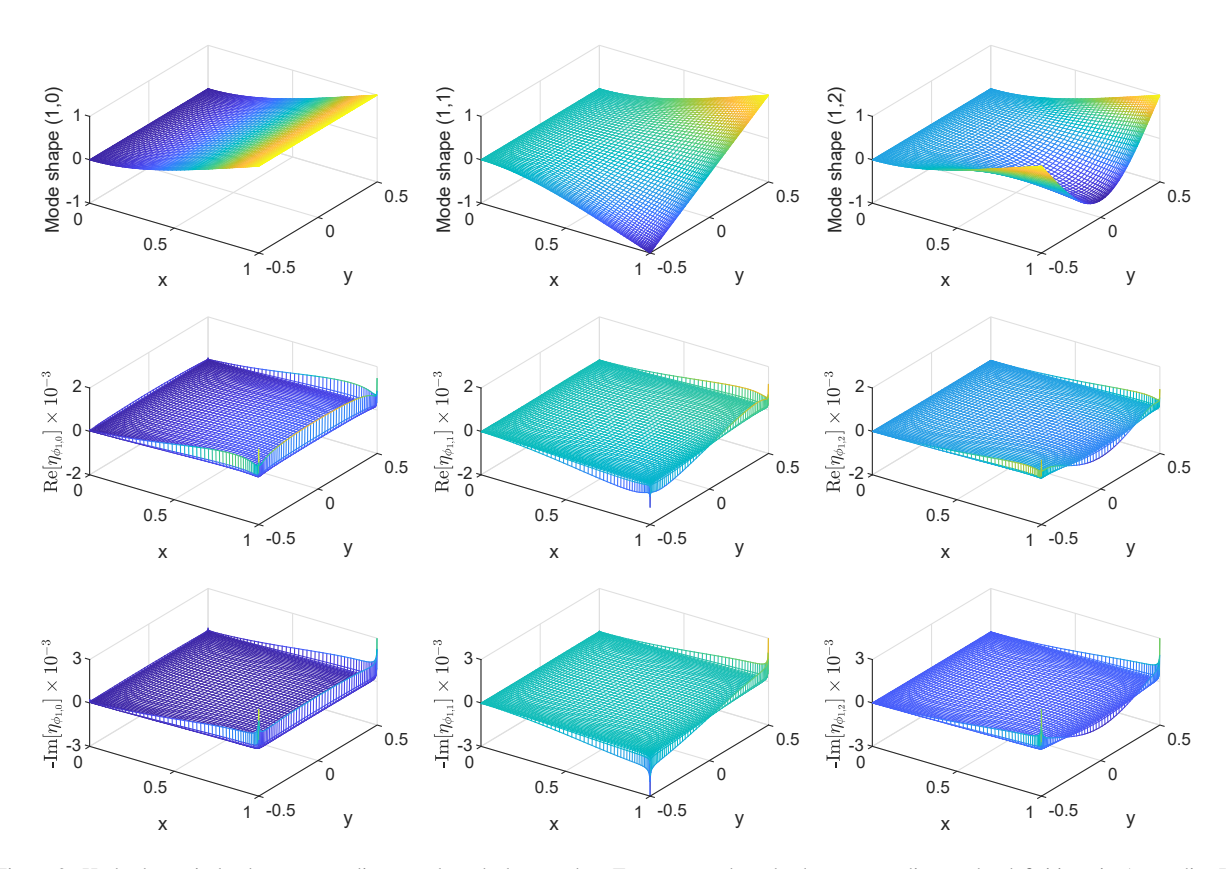


Figure 2: Hydrodynamic loads corresponding to selected plate modes. Top: assumed mode shapes according to the definitions in Appendix B. Middle: real parts of hydrodynamic load phasors. Bottom: Negative imaginary parts of the hydrodynamic load phasors. The frequency parameter is $\alpha = \sqrt{2\pi \cdot 100}$ and the aspect ratio is $\Lambda = 1$, see also Appendix C.2.

As before, this expression is scaled to yield

$$\left[\tilde{\mathbf{K}} - \omega^2 \frac{\rho_s h}{D} \tilde{\mathbf{M}} [\mathbf{I} + \mathcal{R} \tilde{\mathbf{M}}^{-1} \tilde{\mathbf{H}} (\omega)] \hat{\mathbf{q}} (\omega) = \frac{1}{DLb} \hat{\mathbf{f}} (\omega)$$
 (22)

which is the plate counterpart to Eq. (19) derived for a beam in bending. Note that the coefficient $\rho_s h/D$ in Eq. (22) reduces to $\rho_s A/(EI)$ in Eq. (19) if E in the latter is replaced with the Young's modulus in plane strain $E' = E/(1-v^2)$, see also Appendix A. Once the matrices are formed, the equations can be solved for any desired modal forcing and the wet frequency response functions can be formed and compared.

5. Results and discussions

$5.1.\ Nonlocal\ model\ hydrodynamic\ function\ matrix\ as\ solution\ of\ the\ fluids\ problem$

Representative results of the solution of the fluid problem in Eq. (9) are displayed in Fig. 2 which presents the calculated hydrodynamic net traction profiles on a square cantilever plate generated by vibration along three different mode shapes. Results refer to a representative frequency parameter $\alpha = \sqrt{2\pi \cdot 100}$. The selected mode shapes include one cylindrical bending mode (mode (1,0)), one torsional mode (mode (1,1)), and a generic plate mode reminiscent of a shape morphing configuration (mode (1,2)), see [46]. The nomenclature of the plate modes is defined in Appendix B. Within this notation, the second index is also equal to the number of nodes in the y-direction and therefore immediately describes whether the velocity profile is even (as in the cylindrical bending case or in the shape morphing-like mode) or odd (as in the torsion case).

As clearly displayed in the figure, the hydrodynamic loads $\hat{\eta}_{\phi_i}$ are calculated by taking into account the full velocity profile, due to vibrations along mode ϕ_i , of the entire cantilever, with explicit and automatic consideration of

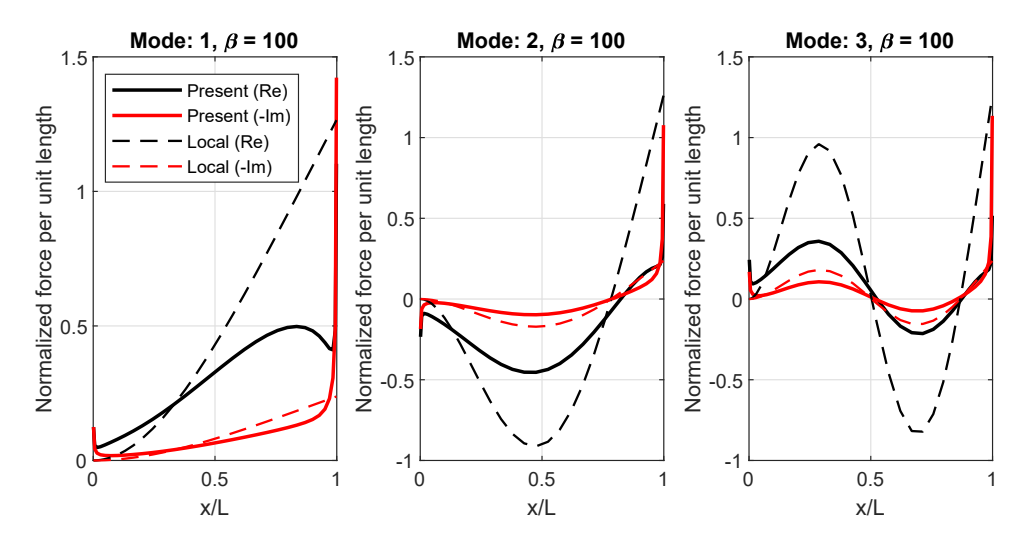


Figure 3: Normalized forces per unit length according to the present nonlocal beam theory and to the local theory, for the first three structural modes of the beam with $\Lambda = 1$. Note how the present theory captures the load singularities due to end effects.

end effects and finite cantilever aspect ratio. It is easy to see that the hydrodynamic load profiles are not proportional to the structural modes, thus rigorously justifying the need of the present nonlocal treatment. Of particular importance are the boundary effects at x = L and especially at the free corners, at $y = \pm b/2$, where the singular behavior of the traction profile becomes prominent. These singularities cannot be captured by the local theory in [22, 1] nor by the recent numerical schemes in [35, 36] which are based on a strip integration method in the chord direction, rather than a fully 3D fluid problem. In addition, our method can seamlessly handle complex plate-like deformations, as it is not restricted to particular functional forms along the x- or y-axis as in [37]. It is also important to notice that the numerical solutions of Eq. (9) shown in Fig. 2 confirm the theoretical predictions of the parity-preserving property, on the even/odd nature of the hydrodynamic load (both for its real and imaginary parts) in response to an even/odd velocity profile for the cantilever as a function of the chord-wise coordinate.

To better illustrate the nonlocal nature of the hydrodynamic load, in Fig. 3 for beam vibrations, we display a comparison of the predictions of the local theory versus the actual forces per unit length obtained by the present approach, as in Eq. (15). In this example, the forces are calculated by applying the hydrodynamic operator on the first three dry beam modes, see Eq. (A.4) in Appendix A. These forces per unit length are obtained by integrating the traction profiles along the chord direction. For ease of presentation, we report results at the representative intermediate nondimensional frequency $\beta = 100$ and aspect ratio $\Lambda = 1$, as in Fig. 2. As shown in Fig. 3, the hydrodynamic forces predicted by the local theory follow closely the mode shapes, while the present theory takes into account the entire deformed shape of the structure. This causes major differences in the way the added mass and damping are included in the calculation, via a severe overestimation. Even though not shown, the deviations of the present formalism from the local theory are more severe as the mode number increases (especially when considering the end effects at the cantilever tip) and typically more pronounced at low β , consistently with the fact that for a more viscous regime, sensitivity to boundary conditions (e.g., motion of the cantilever) extends for larger spatial regions and, consequently, the estimation of hydrodynamic forces progressively becomes a less local problem.

Projecting the nonlocal forces in Fig. 3 on the dry beam modes, we can finally obtain the components of the matrix $H(\omega)$ for beam vibrations, as in Eq. (15). To investigate the non-diagonal nature of the nondimensional operator $\tilde{H}(\beta)$, in Fig. 4 we plot the values of its entries over four decades of nondimensional frequencies $\beta \in [10^0, 10^4]$ for the representative aspect ratios $\Lambda = 5$ in panel (a) and $\Lambda = 1$ in panel (b). Only the components pertinent to the first three modes are reported for brevity, and use is made of the symmetry $\tilde{h}_{ij} = \tilde{h}_{ji}$ for clarity of presentation. In the figure, markers are calculated values while lines represent interpolations at intermediate β values, see Appendix C.2. Black squares and red circles represent the real and the negative imaginary parts, respectively, of the modal hydrodynamic function matrix components. While only the diagonal terms are used in traditional methods calculations, see Eq. (20), it can be seen that off-diagonal terms are non-negligible, constituting up to approximately 10–20%

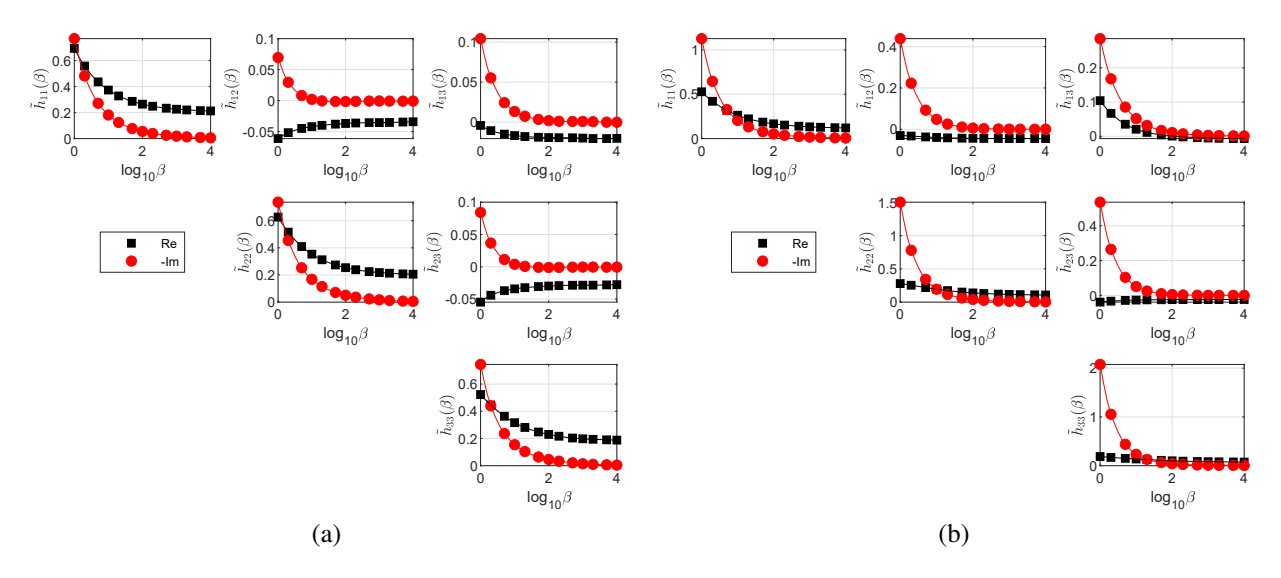


Figure 4: Representative components of the hydrodynamic function matrix $\tilde{\boldsymbol{H}}$ for aspect ratio (a) $\Lambda=5$ and (b) $\Lambda=1$. Note the non-zero off-diagonal components \tilde{h}_{ij} , with $i\neq j$.

of the main diagonal values especially at low frequencies for the imaginary parts for $\Lambda=5$. Interestingly, several off-diagonal terms in the real part take on negative values, which have not been observed in the literature on hydrodynamic functions. However, energy conservation is not violated, as both the real and imaginary parts of $H(\omega)$ are positive definite, for any ω . The contribution of off-diagonal terms is even more substantial for the low aspect ratio case $\Lambda=1$. Here, the off-diagonal terms can reach up to 30–40% of the main diagonal values, thus further indicating the importance of correctly accounting for non-proportionality between displacements and hydrodynamic loads in the structural solution.

5.2. FSI of cantilevered beams

To illustrate the peculiarity of our new nonlocal theory in the context of beam vibrations, in this section, the dynamics in Eq. (19) is solved for the modal coefficients \hat{q}_j by scanning the values of ω (or, equivalently, β) in a frequency band of interest, and the FRF of the system is obtained. In the representative study below, we consider a harmonic unit force load concentrated at the free tip of the cantilever and, where applicable, we consider the response of the system in terms of tip transverse displacements (driving point FRF).

In the following, all results are presented with respect to both the dimensional frequency $f = \omega/(2\pi)$, as well as with respect to two nondimensional frequency axes: the β axis, which emphasizes the hydrodynamic regime for a given frequency band of vibration, and the f^+ axis, which instead emphasizes the structural dynamics aspects of the vibration. Specifically, f^+ is a nondimensional frequency defined as $f^+ = f/f_0$, with $f_0 = \sqrt{Eh^2/(12\rho_s)}/(2\pi L^2)$. Thus, the two nondimensional axes β and f^+ allow direct and immediate comparison of FSI results over broad time and length scales.

First, we assess the effect of neglecting the off-diagonal terms in FSI calculations. Specifically, we study the underwater vibrations of a silicon microcantilever beam ($E=169\,\mathrm{GPa}$, $\nu=0.25$, $\rho_s=2320\,\mathrm{kg/m^3}$, see [41]) with dimensions $L=200\,\mu\mathrm{m}$, $b=40\,\mu\mathrm{m}$, and $h=2\,\mu\mathrm{m}$, so that the aspect ratio is $\Lambda=5$ as in Fig. 4. Fluid properties are taken as $\rho_f=997\,\mathrm{kg/m^3}$ and $\mu_f=8.59\times10^{-4}\,\mathrm{Pa\cdot s}$ for the calculation of β . The first ten modes are used in all calculations. The first two undamped dry modes of the cantilever appear in the frequency range $[0,500]\,\mathrm{kHz}$ ($f^+\approx25$), at approximately $69\,\mathrm{kHz}$ ($f^+\approx3.52$) and $432\,\mathrm{kHz}$ ($f^+\approx22$), along with the first three estimated wet modes as shown in Fig. 5(a). The third dry mode occurs at approximately $1210\,\mathrm{Hz}$ ($f^+\approx61.7$). Note that $120\,\mathrm{Nz}$ corresponds to approximately $120\,\mathrm{Nz}$ and $120\,\mathrm{Nz}$ approximately $120\,\mathrm{Nz}$ app

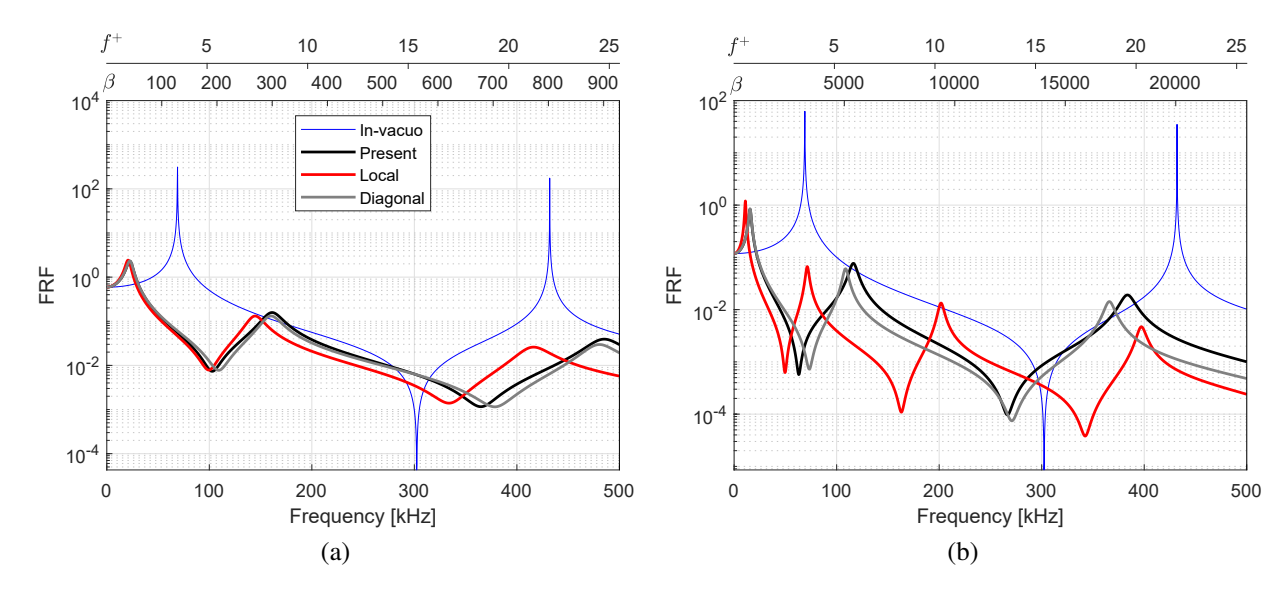


Figure 5: Driving point frequency response function (FRF) for a submerged cantilever beam, elucidating the non-diagonal nature of the hydrodynamic operator and departures from the local theory. In (a), $\Lambda = 5$. In (b), $\Lambda = 1$. FRFs are presented with respect to dimensional frequency, as well as nondimensional parameters β and f^+ to emphasize hydrodynamic and structural regimes, respectively.

unsuccessful as the complicated dependence of the hydrodynamic operator \boldsymbol{H} on ω causes deviations from the typical linear response. Thus, damping is preferentially estimated with the half power points method [60], identifying quality factors as $Q = \omega_p/(\omega_2 - \omega_1)$, where ω_1 and ω_2 are the frequency of the lower and upper half power points, and ω_p is the frequency of the peak response. Similarly, by comparing Eq. (19) with its in vacuo counterpart in Appendix A, we can define the added mass as $M_A = (\omega_d/\omega_w)^2 - 1$, where the subscript d or w indicate dry or wet, respectively, for the resonance frequencies.

In Fig. 5(a), we display the in vacuo driving point FRF (to a concentrated tip load) and the predictions of the classical local theory by Sader [1], along with results from the present approach considering both the full H operator and its "diagonal", but still nonlocal, version, obtained by neglecting off-diagonal entries. Here, R = 6.75. The three approaches predict reasonably close result for the first wet mode frequency and damping (local theory: 20.75 kHz with $M_A = 10.057$, Q = 3.80; present theory: 22.50 kHz with $M_A = 8.404$, Q = 3.62, a difference of approximately 8% in the natural frequencies, approximately around $\beta = 40$ and $\beta = 40$ and $\beta = 1.15$. A slightly larger quality factor and added mass factor are predicted by the local theory.

As expected, more significant discrepancies are progressively observed as the mode number increases. For wet mode 2, at approximately $\beta=300$ and $f^+=8.22$, the local theory predicts a damped resonance at 144.75 kHz with $M_A=7.907$, Q=8.75, while the present theory with full and diagonal hydrodynamic operator suggests 161.25 kHz with $M_A=6.177$, Q=8.57 and 160.25 kHz with $M_A=6.267$, Q=8.75, respectively. The local theory underestimates the natural frequency predicted by the full theory by more than 10%. The diagonal assumption shows discrepancies of less than 1% on the resonance frequency. The local theory and the diagonal assumption also seem to underestimate damping by 2%. For wet mode 3, at approximately $\beta=900$ and $f^+=24.75$, the local theory predicts a damped resonance at 416.40 kHz with $M_A=7.444$, Q=13.47, while the present theory with full and diagonal hydrodynamic operator indicate 485.25 kHz with $M_A=5.218$, Q=14.97 and 480.60 kHz with $M_A=5.339$, Q=15.57, respectively. The local theory and the diagonal assumption underestimate the natural frequency predicted by the full theory by 14% and 1%, respectively.

While $\Lambda = 5$ corresponds to a geometry for which the aspect ratio could be still characteristic of a somewhat slender beam, when considering $\Lambda = 1$ geometry effects should further enhance discrepancies among the local and nonlocal theories. Indeed, this is the case as shown in Fig. 5(b) generated by changing the beam width to b = L. Here, $\mathcal{R} = 33.75$, so the effect of the fluid is expected to be more pronounced as compared to the previous case. While the in vacuo frequencies are not changed (under the assumption that the structural dynamics is governed by the same beam equation), the presence of the fluid has a major effect on the shift of wet natural frequencies and their

Table 1: Frequency response data for a cantilever beam with $\Lambda = 1$. For each mode, natural frequencies are indicated with f_n , added masses with M_A , and quality factors with Q. The columns '% D' indicate percent differences against the present theory.

	Present			Local					Diagonal				
	M_A	f_n (kHz)	Q	M_A	f_n (kHz)	$%$ D f_n	Q	% D Q	M_A	f_n (kHz)	$%$ D f_n	Q	% D Q
Mode 1	18.56	15.6	7.05	38.35	11.00	-29%	10.12	44%	18.56	15.6	0%	7.01	-1%
Mode 2	12.80	116.3	15.22	35.61	71.40	-39%	22.56	48%	14.79	108.7	-7%	20.40	34%
Mode 3	9.04	383.8	23.88	34.95	201.8	-47%	35.46	48%	10.02	364.5	-5%	30.91	29%

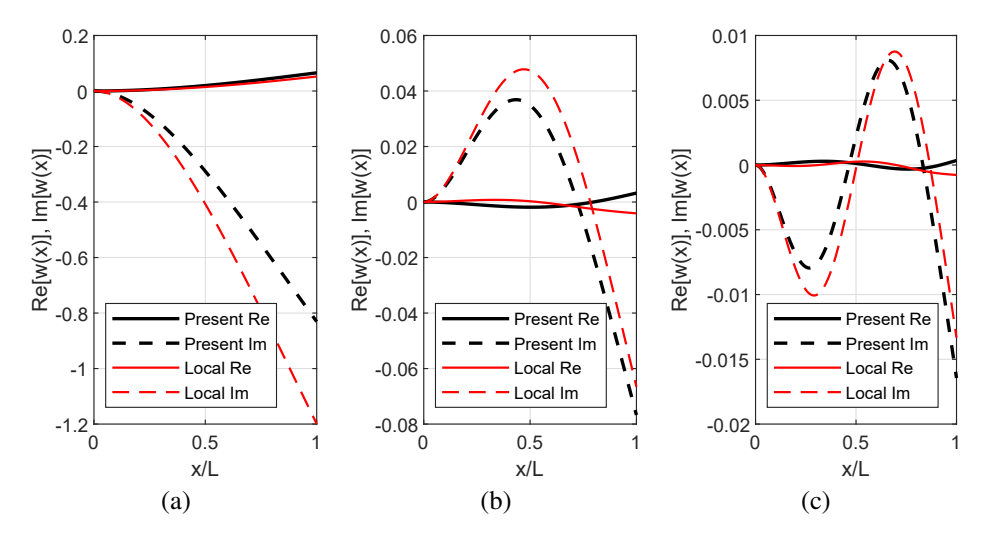


Figure 6: Displacements of the square cantilever, using beam theory, at wet resonance. The real (solid line) and imaginary (dashed line) parts of the deflected shape phasor at resonance. In (a): mode 1, in (b): mode 2, and in (c): mode 3. For the local theory, resonances occur at 11.00, 71.40, and 201.8 kHz. For the present nonlocal theory, resonances occur at 15.6, 116.3, and 383.8 kHz, as in Table 1. Note the shift of the nodal locations and the different vertical axis scale.

associated quality factors. Note that for this problem, 500 kHz corresponds to approximately $\beta=23000$. Since for the $\Lambda=1$ case the values of β are substantially larger than the $\Lambda=5$ case of a factor of 25, the effect of viscosity on hydrodynamic damping is reduced, and the wet peaks appear sharper in Fig. 5(b) as compared to those in Fig. 5(a). Vibrational behavior results are collected in Table 1 which displays significant departures of the present approach from the local theory. Generally speaking, the local theory seems to overestimate the added mass effect, as evidenced by the pronounced low-frequency shift of the resonance frequencies. Interestingly, a fourth mode is predicted in the explored frequency window by the local theory; such mode appears instead outside of the frequency window according to the present approach. The local theory predicts higher quality factors as well, likely by underestimating the effect of hydrodynamic damping due to end effects. As compared to Fig. 5(a), for the $\Lambda=1$ case, the importance of the off-diagonal terms of the operator H becomes more evident and significant underestimation of the hydrodynamic damping could occur by neglecting the off-diagonal components of the modal hydrodynamic function matrix. This finding is entirely consistent with the results shown in Fig. 4. Similarly, the added mass effect appears to be overestimated, possibly due to the presence of negative added mass terms in the full operator, as shown in Fig. 4.

The last observation of this analysis concerns the mode shapes resulting from FSI for the square cantilever under study. In Fig. 6, we display, for the first three wet resonances of the cantilever, the displacement shapes in correspondence of the resonance peaks. These are obtained by constructing a linear combination of the beam modes, weighted by the modal coefficients evaluated at the resonance frequencies determined by the previous analysis. For completeness, we display the real and imaginary part of the displacements, while observing that, because one of the landmarks of resonance is the fact that displacement and excitation are in quadrature of phase (i.e., $\pi/2$ apart), the largest contribution to the absolute value of displacement is provided by the imaginary part. It can be seen that the mode shapes are modified by the nonlocal treatment of the hydrodynamic loading and such modifications are more evident for the higher structural modes. This observation is made clear by the shift of the nodal positions along the beam axis that can be easily identified in panels (b) and (c) of Fig. 6. This result highlights an important methodological difference between our work and [46], in that the wet mode shapes cannot be imposed a priori, but they will be a result of the

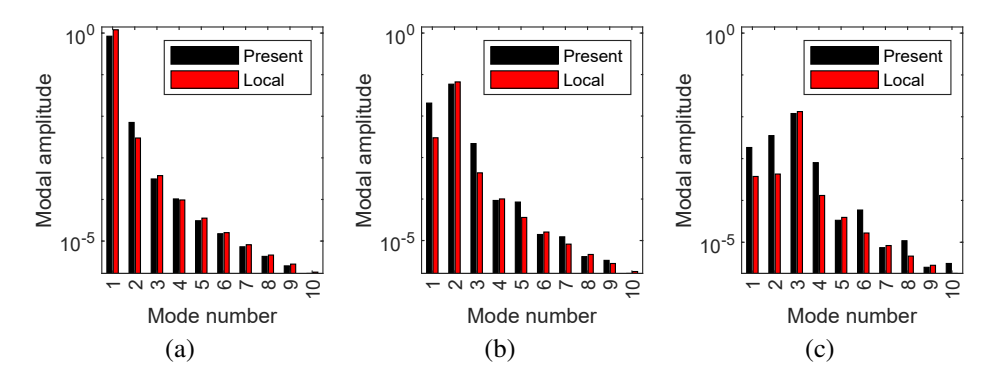


Figure 7: Magnitudes (in log scale) of the modal coefficients \hat{q}_i at wet resonance for the square cantilever $\Lambda = 1$. In (a): mode 1, in (b); mode 2, and in (c): mode (3).

overall forcing on the structure.

The fact that many dry modes can contribute to the wet shape can be quantitatively ascertained by evaluating the modal coefficients at wet resonance, as shown in Fig. 7. For this particular case of reasonably well-spaced modes, it can be seen that the *i*-th dry mode is the main contributor to the corresponding *i*-th wet shape. However, the relative contribution of the other modes is not negligible in the prediction of the present theory. We remark in particular, for the second and third mode, the contribution of the lower modes (whose amplitude is of the same order of the main harmonic) and the comparatively slow decay of the higher modes, as opposed to the local theory. This strong coupling effect likely stems from the non-diagonal nature of the hydrodynamic function matrix and its capability of exciting otherwise orthogonal modes.

5.3. FSI of cantilevered plates

Many of the general conclusions of the previous subsection can be repeated for the plate case. However, here we will primarily focus on the unique predictions of the plate theory against those of the beam theory. First, we consider in Fig. 8(a) a relatively slender cantilever plate case with $\Lambda = 5$, with the same geometric and material properties as in the previous section, for ease of comparison. The plate is loaded with a unit force at the corner (x = L, y = b/2)and the driving point FRF is displayed. The problem is treated with both the plate theory of this section and the beam theory of the previous section to highlight similarities and differences. In Fig. 8(a) we also display the predicted in vacuo responses for the plate, the beam, and the torsional theory of beams in Appendix A. For completeness, we superimpose to the dry and the wet responses calculated with the present nonlocal theory also the predictions of the local theory of [1] for beams in bending and of [24] for beams in torsion. Note that the beam model is loaded with a unit harmonic force at the tip (x = L) as it is not possible to specify in that theory the dependence on y; vice versa, the beam in torsion is loaded with a harmonic tip moment of numerical magnitude (b/2), to replicate the moment of the unit corner load in the plate problem. The chosen loading profiles make the response immediately comparable among each other and, importantly, allow the excitation of all modes in the plate problem. The frequency response are shown in the band 0–2000 kHz ($f^+ \approx 100$), encompassing the first few wet modes of the plate. For this relatively slender cantilever, the predictions of the nonlocal beam theory are essentially coincident with those of the nonlocal plate theory for the first two bending modes (at approximately 23 kHz or $f^+ = 1.17$ and 163 kHz or $f^+ = 8.3$). For the next three bending modes (at 495 kHz or f^+ = 25.2, 1023 kHz or f^+ = 52.2, and 1788 kHz or f^+ = 91.2), the local beam theory increasingly underestimates the natural frequencies of the nonlocal plate theory. The local beam theory predictions are consistently severely underestimating the nonlocal results of this work starting from the third bending mode. Interestingly, the nonlocal plate theory seamlessly captures the torsional behavior (and in fact, more general plate-like behavior) as shown by the superimposed predictions of the ad-hoc "mechanics of materials" torsion theory in [24]. The discrepancies in the first wet torsional mode (at 354 kHz or f^+ = 18.1) between the local and nonlocal theory can in part be ascribed to the differences in the predictions of the in vacuo torsional frequencies, that seem to be underestimated by the local torsional beam theory. Higher order torsional modes (at 1131 kHz or f^+ = 57.7 and 1989 kHz or f^+ = 101.4) are progressively misidentified by the local theory. Another feature of the plate theory is that it seems to consistently suggest higher quality factors for the resonant peaks when compared to the beam theories,

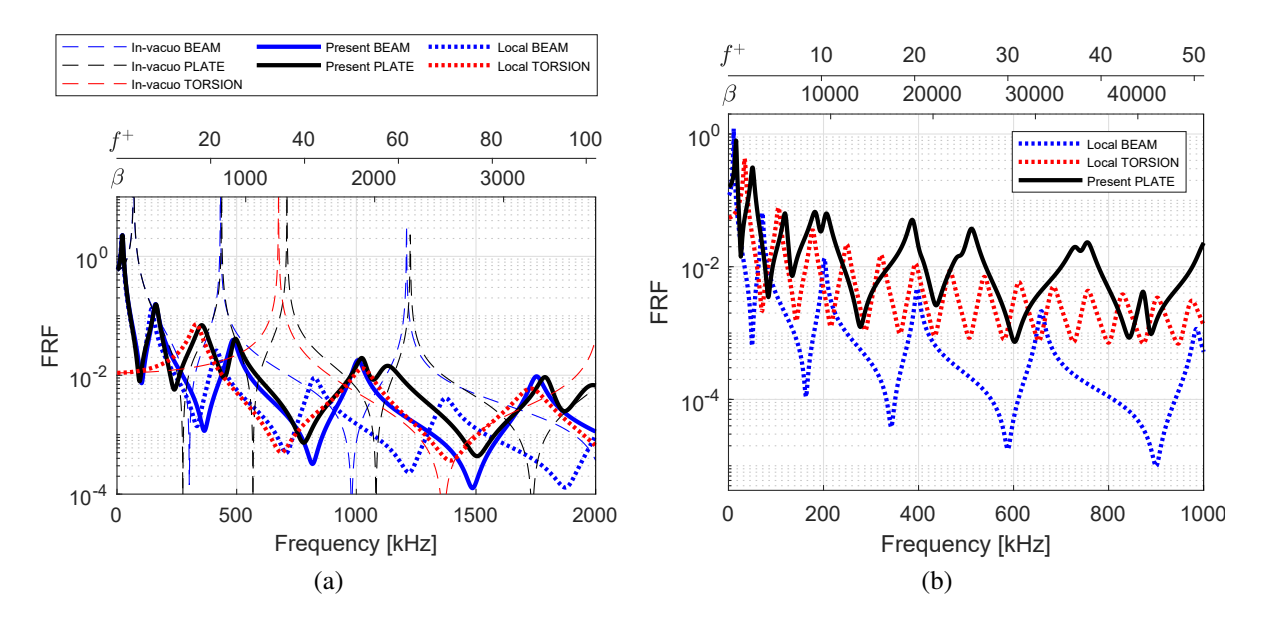


Figure 8: FRF for a microplate with aspect ratio (a): $\Lambda = 5$, and (b): $\Lambda = 1$. In (a), the figure shows the in vacuo responses (dashed lines) for beam in bending, beam in torsion, and plate behavior; predictions of the present nonlocal theory (thick lines) for beam and plate behavior; and predictions of the local theory (dotted lines) for beams in bending and torsion. In (b), only a subset of the responses is shown for clarity. FRFs are presented with respect to dimensional frequency, as well as nondimensional parameters β and f^+ to emphasize hydrodynamic and structural regimes, respectively.

except for the first bending mode. This result should not however be ascribed to the use of a Young's modulus in plane strain for the plate (embedded in the rigidity D) versus a Young's modulus in plane stress for the beam, as the first in vacuo bending frequencies are virtually coincident.

A similar analysis is conducted on a square plate (same as above but with $b = 200 \,\mu\text{m}$) with aspect ratio $\Lambda = 1$. For this more "extreme" aspect ratio, results are qualitatively displayed in Fig. 8(b). For this aspect ratio, the hypotheses of the local theory are expected to break down even for low mode numbers. Due to the high density of resonances in the window 0–2000 kHz, we choose to only report the predictions of our present nonlocal plate theory against those of the local theories for bending and torsion in the band 0–1000 kHz. Qualitatively, we conclude that, with possibly the exception of the first bending mode, the dynamic behavior cannot be reliably identified by local beam theories, thus demonstrating the need of a full nonlocal plate theory for low aspect ratios and higher mode numbers.

This conclusion can be also reached by considering the mode shapes at wet resonance, as displayed in Fig. 9. It is important to note that the mode shapes here are damped (by the actions of the fluid) and therefore described by complex-valued vectors. The shapes depicted in Fig. 9 are then the particular shape of the plate at resonance, at a specific instant of time. Because of the complex nature of these modes, the nodal lines shift in the plate domain during a vibration cycle. At any rate, even for the first ten resonances, coincident with those displayed in the FRF of Fig. 8(b), the complexity of the actual shapes demonstrates that assuming that a plate is undergoing a prescribed cylindrical bending, torsion, or any other prototypical deformation along the *x*- or *y*-directions, imposes an unrealistic constraint on the dynamic behavior of the system which is therefore reflected in significant errors in the estimation of its spectral characteristics.

One may argue that the inadequacy of the beam theories stems from the fact that in the case presented the structure is excited with a corner force, a situation that cannot be rigorously captured with the 1D descriptions of beam theories, and thus that the discussion above may be an unfair comparison. However, the results for $\Lambda = 5$ do not support this conclusion. As additional supporting argument, we present in Fig. 10 the first few modes in underwater resonance due to the so-called "even" (or symmetric) and "odd" (or antisymmetric) excitations discussed in [35] and due to a uniform harmonic pressure on the plate. The even and odd excitations are constructed by applying to the plate free corners at $y = \pm b/2$ a pair of forces either in phase (even excitation) or out of phase (odd excitation) with each other.

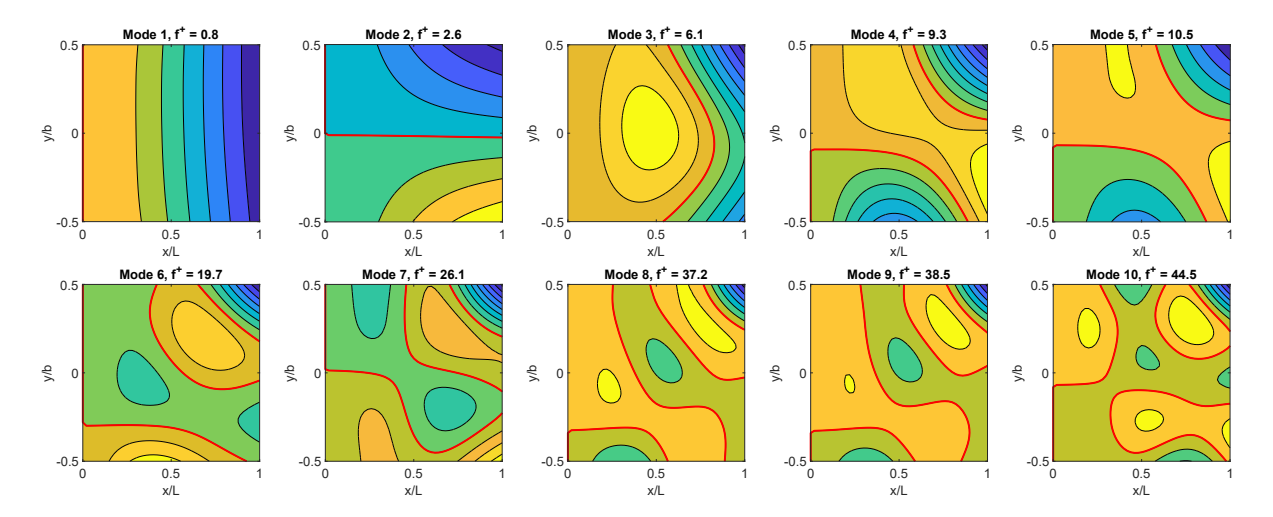


Figure 9: First ten wet forced resonances for the square plate excited by a corner force, as in Fig. 8(b). Mode number and frequencies are indicated. Thick red lines denote the nodal lines at the shown instant of time.

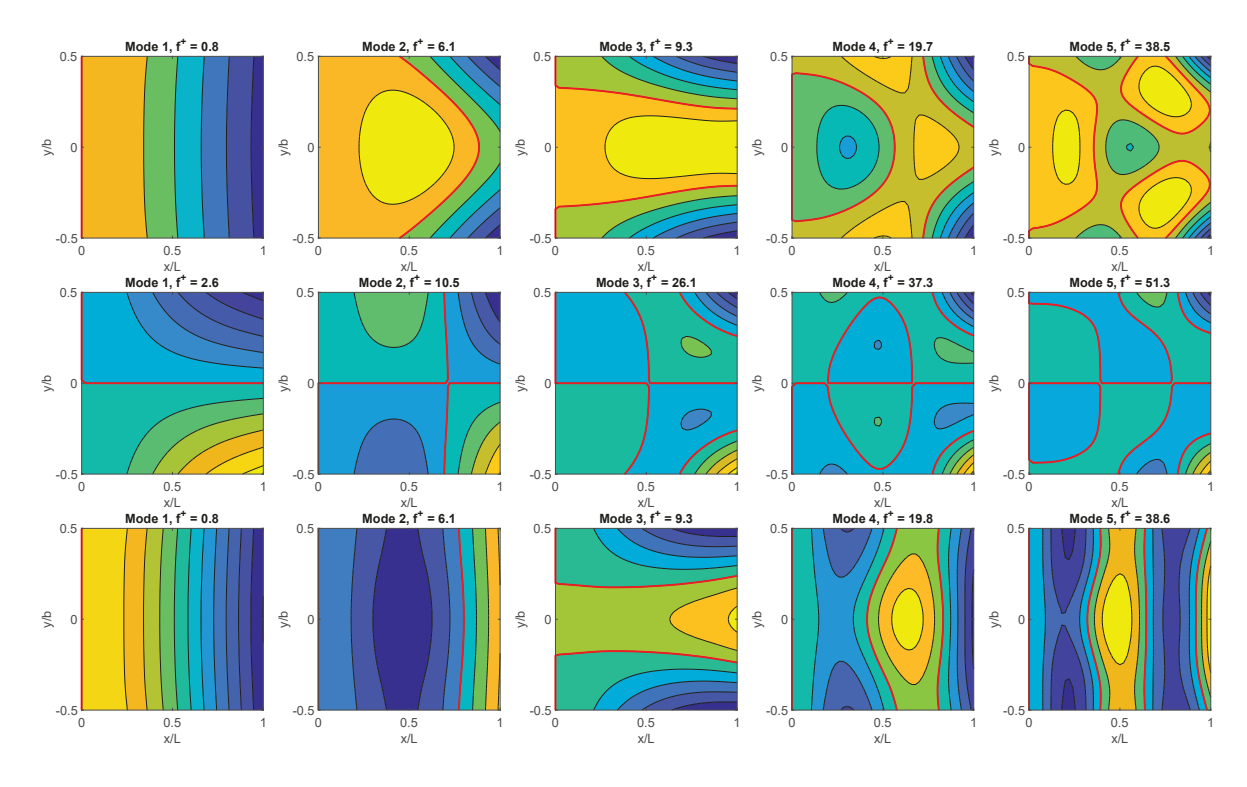


Figure 10: First five wet forced resonances for the square plate under (top) even, (middle) odd, and (bottom) uniform excitation. Mode number and frequencies are indicated. Thick red lines denote the nodal lines at the shown instant of time. Note the plate-like nature of the excited modes and the marked y-dependence that beam theories cannot capture.

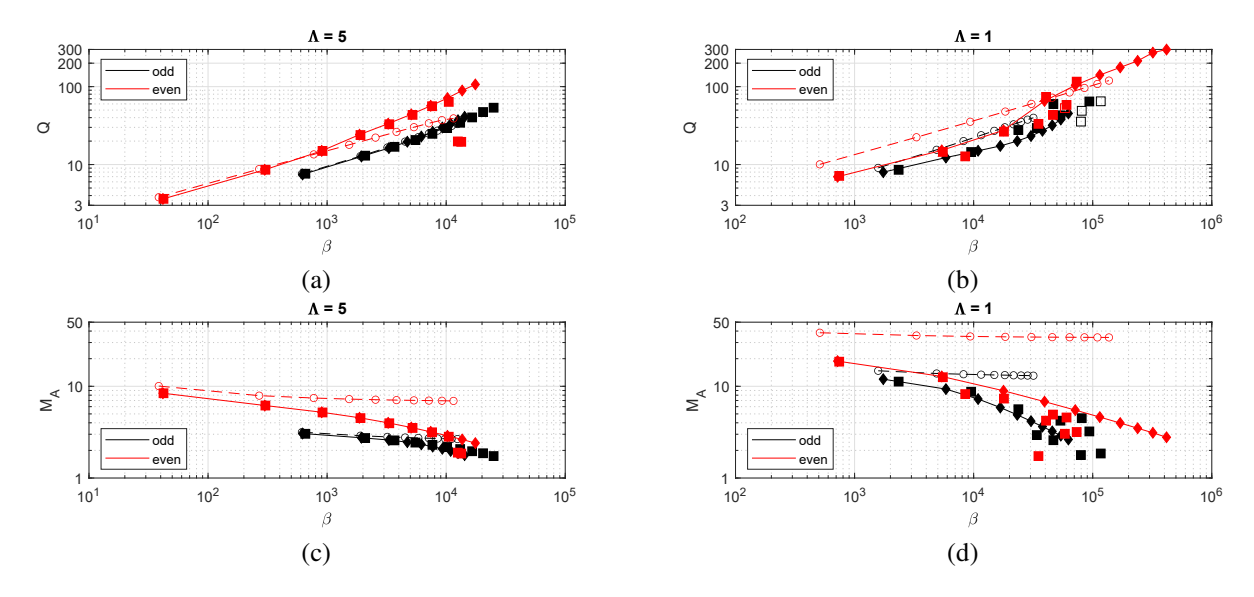


Figure 11: Quality factors Q for (a) $\Lambda = 5$ and and (b) $\Lambda = 1$. Added mass coefficients M_A for (c) $\Lambda = 5$ and and (d) $\Lambda = 1$. Red and black markers indicate even and odd excitations, respectively. Empty circles refer to the local beam theory. Filled diamonds refer to the nonlocal beam theory. Filled squares refer to the nonlocal plate theory. The dashed lines (local beam theory) and the solid lines (nonlocal beam theory) are only meant as a visual guide.

It can be seen in Fig. 10 that, beside the very first resonance, these simple excitation profiles fail to excite exclusively beam-like modes (e.g. cylindrical bending or torsion). Instead, a marked nontrivial y-dependence of the shapes can be observed for all but the simplest cases. Thus, the hypothesis of fluid-structure interactions stemming from prescribed beam-like mode shapes independent of the y-coordinate must be understood as a strong one. We also remark here that an even (odd) excitation only produces an even (odd) structural response, consistently with the discussion of the even or odd nature of the hydrodynamic loading.

5.4. Quantitative exploration of the frequency response functions

Due to the complexity and density of the spectral data, rather than displaying results in the form of frequency response functions, in the following we investigate the predictions of the present theories by considering added mass coefficients and quality factors for two separate aspect ratios and fluid loading scenarios. For this purpose, we present quality factors and added masses of submerged cantilevers for $\Lambda = 5$ in Fig. 11(a) and (c), respectively, and $\Lambda = 1$ in Fig. 11(b) and (d), respectively. The cantilevers are forced with odd and even excitations as described in the previous section. Results are reported for the classical local beam theory, as well as for the nonlocal beam and nonlocal plate theories of this work. In the figures, red and black symbols and lines refer to even and odd excitations, respectively. Empty markers and dashed lines denote the values for the local beam theory. Filled diamonds and solid lines denote the value for the nonlocal beam theory. Finally, filled squares represent the values predicted by the nonlocal plate theory. While the quality factors have been calculated with the half power points technique described above, we should note that this identification fails for a few closely spaced modes. For the cases in Fig. 11(b) indicated by empty square symbols where the identification fails, the quality factors are identified from the FRF by fitting the response of a single degree of freedom damped oscillator, as for example described in [41].

In Fig. 11(a) and (c), the quality factors and added masses are presented for $\Lambda=5$. Trendlines are included in the figure to aid visual interpretation. In Fig. 11(a), the local beam theory and nonlocal beam theory show agreement on first two modes for both even and odd excitations. For the case of even excitation, the local beam theory and the nonlocal beam theory predict quality factors of 3.80 vs. 3.62 and 8.75 vs. 8.57 for the first two modes. For the odd excitation, the local beam theory and the nonlocal beam theory estimate quality factors as 7.58 vs. 7.46 and 12.82 vs. 12.68, respectively. On the other hand, the plate theory estimates these values as 3.63 and 8.57 for the first two modes for even excitation, and 7.63 and 13 for the first two modes for odd excitation. For even excitation, after the third mode, the nonlocal beam theory departs from the linear behavior in log-log scale of the local one, showing a faster

growth as a function of β . The nonlocal plate theory follows the nonlocal beam predictions closely, except for the ninth and tenth modes. For this relatively slender structure, plate modes and beam modes are qualitatively similar, thus explaining the similarity in the response. For relatively simple beam-like shapes, the Q factors seem largely dependent on the vibration frequency only, an observation that can be explained by considering the generally lower values of the hydrodynamic traction as the number of nodal lines increase (which enforce regions of zero velocity boundary conditions), see also Fig. 2. Odd modes are more damped than the even ones, consistently with the predictions of the local theory, as well. A possible explanation for this can be sought in the effect of the singularities in the imaginary part of the hydrodynamic load. These high intensity load profiles are concentrated in a small region in the vicinity of the free edges of the structure, where they can contribute to large damping moment, see also Fig 2. A correspondingly large damping force is not generated for the case of even modes due to the small support of these singularities.

In Fig. 11(c), for even excitation, added masses of nonlocal beam and plate theories exhibit excellent agreement with a general decreasing trend as β increases. Along this trend, the nonlocal beam theory predicts the first and the eighth added masses coefficients as 8.4 and 2.88, whereas the plate theory suggests the close values of 8.4 and 2.82. However, the behavior of the local theory is markedly different, displaying much less sensitivity with respect to β , with values that vary only between 10.06 to 6.93 over almost three decades of nondimensional frequency. For the odd excitation case, the three theories are somewhat closer to each other, again probably due to the presence of the nodal line at y = 0. Specifically, the local beam, nonlocal beam, and nonlocal plate theories estimate the first added masses of the first two modes as 3.16 and 2.89, 3.06 and 2.75, and 3.03 and 2.73. The local beam theory shows a mildly decreasing trend where its tenth added mass value is $M_A = 2.66$. The nonlocal beam and plate theories predict a more marked effect of the fluid, possibly through the non-diagonal nature of the hydrodynamic operator, estimating their tenth added mass value as $M_A = 1.77$ and $M_A = 1.73$, respectively.

Figures 11(b) and (d) show the quality factors and added masses for the low aspect ratio $\Lambda = 1$. Note that the nondimensional frequency β range explored in this case is approximately one decade larger than that of the $\Lambda=5$ case. At a glance, we expect therefore higher quality factors due to the less viscous nature of the fluid at high β , as well as lower added mass coefficients. However, the effect of the frequency increase is in part balanced by the larger value of \mathcal{R} for the low aspect ratio structure, which is thus more heavily affected by the presence of the fluid. In this case, one can immediately see that the nonlocal beam and plate theories demonstrate very different characteristics from the local theory for both even and odd excitations. In Fig. 11(b), for even excitation, the nonlocal beam and plate theories have comparable quality factors for the first two modes as 6.97 vs. 7.15 and 15.21 vs. 14.52. However, the first two mode predictions of the local beam theory are 10.06 and 22.4, significantly far off from our novel theories. Contrary to the apparent linear behavior of local beam theory in log-log scale (again, an effect of the dependence on β only as postulated in [1]), the prediction of the nonlocal beam theory on the quality factors shows a faster increase from the third mode to the fourth mode. For the plate theory, on the other hand, the key effect of correctly accounting for the y-dependence on low aspect ratios, causes the mode shapes to become very complex and the quality factors to be scattered without any strongly identifiable trend, except the general increase of the quality factor as the fluid regime becomes less viscous. Some values show similarity to the estimations of the nonlocal beam theory, especially where the bending-like modes are dominant. This is the case for example in the third mode of the nonlocal beam theory and the fourth mode of the plate theory. For odd excitation, the nonlocal beam and plate theories have similar quality factors for the first two modes as 8 vs. 8.56 and 12.3 vs. 14.48. After the second mode, the nonlocal beam theory shows an increasing slope up to tenth mode with Q = 45.3. The quality factors for the plate theory are increasingly scattered after approximately the fourth mode.

For the added masses coefficients in Fig. 11(d), the characteristics of the three theories follow qualitatively what described above, as the local beam theory predictions are very different than the other theories. In particular, only mild dependence on β is observed as the values of M_A decrease from 38 to 34 and from 15 to 13 for even and odd excitations, respectively. Added masses of the nonlocal beam and plate theories exhibit excellent agreement for the first two modes with 18.81 vs. 18.55 and 12.81 vs. 12.56 for the even excitation and 11.96 vs. 11.25 and 9.31 vs. 8.71 for the odd excitation. After approximately the second mode, predictions of the nonlocal beam theory follow a well-defined decreasing trend, while the plate theory shows large scatter, for both even and odd excitations. Again, both theories exhibit similar added masses for those modes in which bending is dominant.

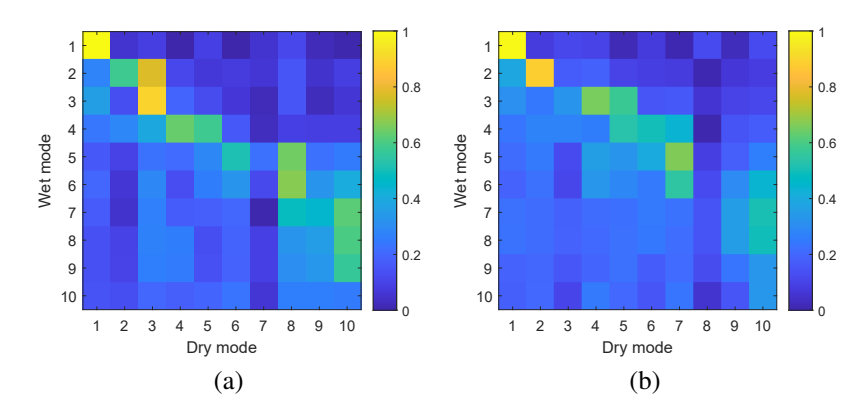


Figure 12: Coherence maps between dry and wet modes for aspect ratio $\Lambda = 1$. In (a): even excitation; in (b): odd excitation.

5.5. Relationship between dry and wet plate modes

Figure 11 fundamentally summarizes how our novel theories behave differently than the local approaches and further indicates the limitation of beam theories for low aspect ratios. Specifically, the quality factors generally increase as β increases, consistently with the less viscous behavior of the fluid. They also largely depend only on the frequency of the resonance and, for sufficiently spaced modes, they generally fall along an approximate trendline for the high aspect ratio case, where beam-like modes are dominant. In this case, also for the plate-like modes qualitative separation between the trends for odd or even excitation is well-defined. This separation and the trendlines worsen for low aspect ratio to the point that no definite trend characteristic can be defined for the $\Lambda = 1$ case. This peculiar situation can be understood by referring to the complicated mode shapes of the response at wet resonance in Fig. 10. Clearly, the changes in mode shape can be fairly dramatic when the mode number increases and a clean scaling law of the Q factors is not be expected as the details of the mode shape significantly influence the hydrodynamic response, and vice versa. Similar conclusions can be drawn for the cases of the added mass, with particular reference to the scattered distribution of the M_A values in Fig. 11(d) for $\Lambda = 1$.

Additionally, one important yet subtle complication stems from the fact that the M_A terms are calculated by comparing the dry response versus the wet dynamics. In an effort to understand the complicated scatter of these coefficients, we discover that the dry modes (or, more properly, shapes at resonance) Ψ_i^d of the structure are qualitatively different from the wet modes Ψ_i^w , generally in a non-trivial way. First, we remark again that, while the dry modes are real-valued vectors, the wet modes are actually complex-valued vectors and as such their shape changes over the vibration cycle. Particularly, and as expected, the nodal locations shift over the plate in a wave-like fashion during the vibration. For few lowest structural modes it is still possible to qualitatively track how the, say, i-th mode gets mapped to the i'-th wet mode and, often, i = i'. However, beyond the first few pairs (especially for low aspect ratio plates), the modes are too different to be qualitatively matched, see also the examples in Figs. 9 and 10.

We resort then to a quantitative mode tracking algorithm, that is in part inspired by [42]. We calculate a "coherence" factor as the absolute value of the normalized dot product between a wet and a dry mode according to

$$\gamma_{ij} = |(\Psi_i^d)^* \Psi_i^w| / (||\Psi_i^d|| \, ||\Psi_i^w||) \tag{23}$$

With this definition, the correlation γ_{ij} is equal to 1 if the shape of the dry mode i is identical over the vibration period to that of the wet mode j, and 0 if they are completely uncorrelated (orthogonal). Numerical experimentation shows that this definition is particularly suited to compare complex-valued modes as it is insensitive to the phase angle between the wet and dry modes. The same conclusion does not hold true if a traditional "cosine" of the angle between the vectors is considered, which could yield values between -1 and 1 depending on the phase shift between the vectors, which however is inconsequential in this discussion. The coherence maps are displayed in Fig. 12 for the case of even and odd excitation for $\Lambda = 1$. Lighter cells in the matrix plot indicate high level of coherence between dry and wet modes. Clustering along the main diagonal suggests general mapping of dry mode i to wet mode j with i = j. Unfortunately, the mapping is not one-to-one so that, especially for closely spaced modes, several dry modes i, i', etc. may be mapped to the same j wet mode. This contributes to adding to the complexity of the problem.

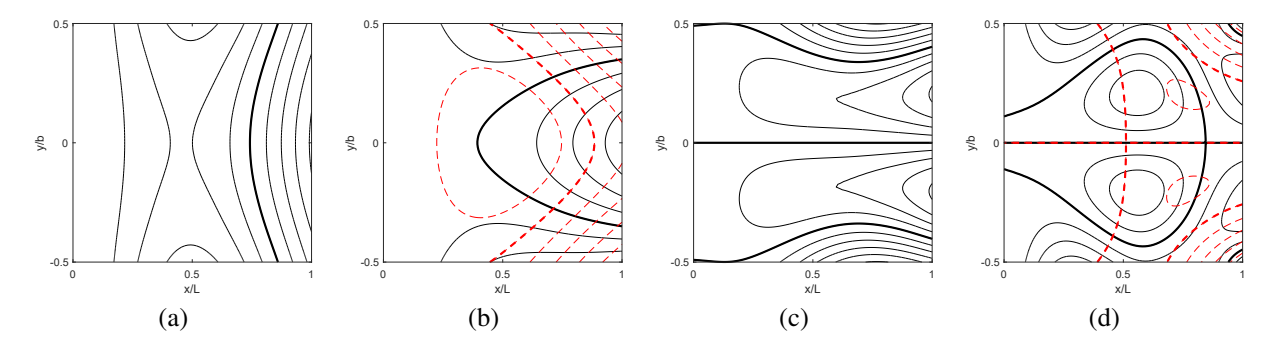


Figure 13: Contour plots of dry versus wet low coherence modes for the square plate. In (a) and (b): dry and wet mode 2 under even excitation, respectively; in (c) and (d): dry and wet mode 3 under odd excitation, respectively. Solid lines: contours of real parts. Dashed lines: contours of imaginary parts (for wet modes). Thick lines show nodal lines.

Even more interesting is the apparent observation that some dry modes do not seem to have a definite wet counterpart, even for low mode order. We study in particular the low coherence cases of second dry mode under even excitation, for which $\gamma_{22} = 0.58$, and the third dry mode under odd excitation, for which $\gamma_{33} = 0.33$, as displayed in Fig. 13. Because of the fluid-structure interactions, the correspondence between structural modes is completely unrecognizable. This observation suggests that assuming a prescribed structural shape for the hydrodynamics calculations, informed by the dry modes of the structure, should be understood as a strong working hypothesis, whose accuracy should be carefully addressed in the general case.

5.6. Flow fields generated by the vibration

To further clarify the hydrodynamics effects in the fully coupled problem and to demonstrate additional capabilities of our model, we briefly discuss below representative flow fields generated by the fully coupled vibrations of the square cantilever plate in correspondence of the two low-coherence modes identified above. The flow fields are efficiently calculated via the boundary element method analysis described above. In particular, from the solution of the fully coupled FSI problem in Eq. (22), we first determine the modal coefficients $\hat{q}(\omega)$ at the frequency of interest. These are used to reconstruct the displacement profile \hat{w} via the modal decomposition and to calculate, via Eq. (9), the traction $[[\hat{\tau}]]$ across the plate domain. Once the traction is calculated, flow variables of interest, including velocity components, vorticity components, as well as components of the velocity gradient tensor, can be calculated, at points of interest in a 3D fluid grid, via the unsteady singularities reported in Appendix C.1. The resulting flow fields can then be plotted to better understand the flow physics generated by the plate vibrations. Remarkably, because the treatment is based on phasor quantities, any flow variable can be calculated at any time during the vibration cycle as, say for example, $u(t) = \text{Im}\left[\hat{u}\exp(i\omega t)\right]$ to construct a detailed time evolution description of the physical quantities of interest.

In Figs. 14(a) and (b), we present the 3D flow fields generated by the plate vibrations at the second resonance peak for the even excitation (as in Fig. 13(b)) and at the third resonance peak for the odd excitation (as in Fig. 13(d)), respectively. For illustration purpose, we display isosurfaces of vorticity magnitude contours, colored by values of the Q-criterion, i.e. the second invariant of the velocity gradient tensor [61], superimposed to velocity streamlines and a slice plot of the axial velocity profile along the plate, for each case. Note that positive values of the Q-criterion identify the presence of vortices in the flow. The undeformed configuration of the plate is indicated via the gray rectangle in the *xy*-plane.

Fig. 14(a) displays details of the 3D flow field pertaining to a vibration mode reminiscent of a so-called "shape-morphing" deformation [43, 46], in this case produced by the even excitation profile. The deformed shape is properly plate-like, with nonzero spanwise and chordwise curvatures. Interestingly, while the corresponding dry mode is characterized by generally negative Gaussian curvature (product of the principal curvatures) so that the plate "looks" like a saddle, the wet mode under study has predominantly positive Gaussian curvature throughout the vibration cycle. This substantial change is due to the presence of the fluid and is reflected in the low coherence highlighted above. Focusing on the flow field at the time instant shown, characterized by a nondimensional frequency parameter approximately equal to $\beta \sim 5 \times 10^3$, the vorticity magnitude contours of the flow field display symmetry with respect to the plane y = 0, due to the even excitation. We note the existence of two vortex tubes around the free edges of

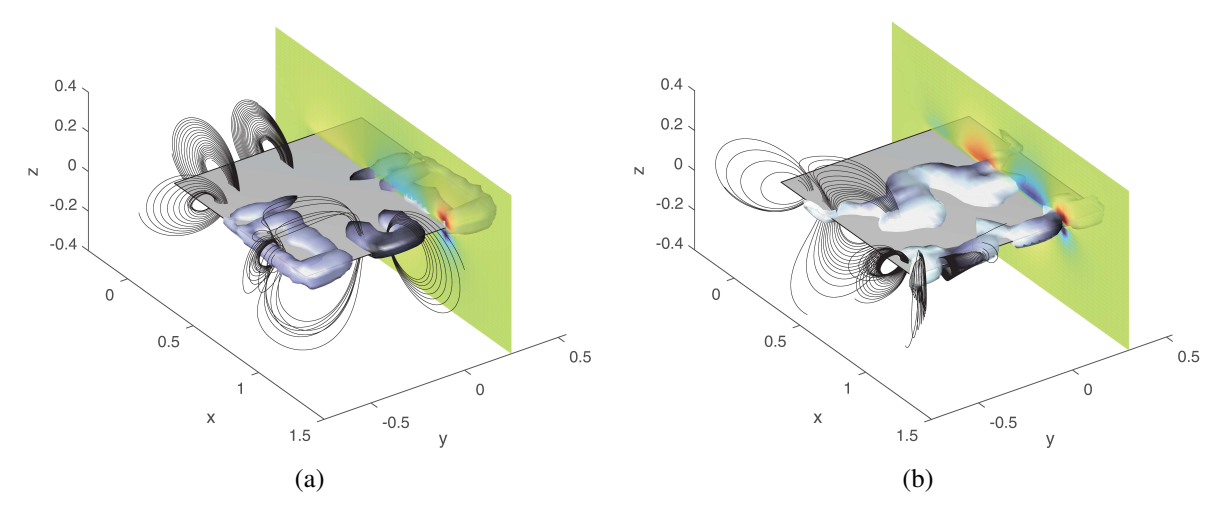


Figure 14: 3D flow fields generated by the square plate vibration for: a) the second mode for even excitation; and b) the third mode for odd excitation. Isosurfaces of vorticity magnitude contours are colored by the values of Q-criterion (light areas indicate positive Q-values), superimposed to selected streamlines and velocity profiles. Note the complicated nature of the flow that cannot be captured via the 2D fluid approximation in the yz-plane.

the plate as indicated by the lightly colored surfaces indicating a positive value of Q-criterion. Notice that the flow is highly 3D and the magnitude of the vorticity is the highest on the corners, as it can be also inferred from the pressure profile in Fig. 2. A third high-vorticity region envelops the free edge at x = L, and is purely a 3D effect that is completely neglected by 2D fluid approximations. The streamlines of the field reveal substantial complexity of the seemingly simple symmetric flow. First, all streamlines are narrowly spaced close to the plate surface, as it is expected since the vibrations of the plate are the main source of motion. Further away from the surface, the streamlines around the clamped edge of the plate, where the motion of the plate is zero, display dissimilar and non-planar trajectories, hinting to important 3D flow effects even in the region away from the gross fluid motion. In the middle of the plate, the severity of 3D flow increases and on the corner of the plate, the flow becomes highly complex. Finally, the slice plot of the axial velocity profile further demonstrates the 3D nature of the flow, in particular showcasing non-zero velocity values along the x-axis. These results confirm our fundamental hypothesis that 2D fluid approximations in the yz-plane, set forth in most local approaches, are inadequate to accurately study the dynamics of these highly complex flows.

Similarly, in Fig. 14(b), the mode shape shown corresponds to a complicated torsion-like motion with a nodal line along the x-axis of the plate, at a nondimensional frequency parameter approximately equal to $\beta \sim 2 \times 10^4$. As expected from a torsional mode of the plate, the flow is antisymmetric with respect to the y-axis. The contours of vorticity magnitude shows symmetry with respect to the y=0 plane and larger magnitude at the free corners of the plate, where larger displacements and velocities (and their gradients) are expected, see also Fig. 13(d). The streamlines again highlight the highly 3D and complex flow on the surface, at the edges and corners of the plate. The existence of a complicated axial flow profile is further demonstrated by the slice plot.

While the two examples in this section are chosen to further investigate the effect of the fluid on the low-coherence modes, 3D flow is observed, to varying degree, in all dynamic conditions.

5.7. Comparison with Experiments

Finally, we propose a comparison of the predictions of the present nonlocal theory against experimental results on in-air and underwater vibrations of a square plate. Although the previous discussion focused on microscale systems to better highlight viscosity effects, the experiments are conducted here at the macroscale, see Fig. 15(a). Specifically, our test article comprises a thin PVC square of dimensions $40 \times 40 \text{ mm}^2$ obtained from a sheet of thickness approximately measured to h = 0.35 mm. The article is weighed to determine its mass via direct measurement. The density, obtained by dividing the mass by the total volume of the article is found to be approximately $\rho_s = 1372 \text{ kg/m}^3$. The test article is rigidly connected via its fixed edge to an electrodynamic shaker actuated by a function generator. A sinusoidal

displacement is applied to the plate base and the motion of the plate is acquired via a high speed camera. A continuous wave 532 nm green laser is used to illuminate the cantilever cross section in the field of view of the camera. A point on the fixed edge and one of the free corners of the plate are tracked via image-based video analysis via the software package Tracker [62], to determine the time history of their absolute displacement, respectively $W_B(t)$ and $W_C(t)$. The elastic motion of the corner (removing the rigid body motion of the base) is estimated via $w_C(t) = W_C(t) - W_B(t)$. We then determine phasors for the corner elastic deformation \hat{w}_C and the base motion \hat{W}_B and calculate the relevant FRF magnitude as $|\hat{w}_C/\hat{W}_B|$. In the data analysis, phasors are identified over a moving time window spanning approximately 3 vibration cycles; several values of the phasors are therefore identified over the entire duration of the experiments. These values are used to determine average and standard deviation of the responses. In the identification, some of the data presented display relatively large standard deviations, a result of the technical difficulties of correctly capturing via imaging the very small amplitudes of the base excitation. However, the data scatter does not affect the conclusions of the experimental campaign.

The explored range of frequencies, between 0–400 Hz, includes the first two in-air bending modes, as well as the first in-air torsion mode of the plate. The amplitude of the excitation is kept sufficiently low to avoid nonlinearities in the response. Experiments are first conducted in-air, to identify the first and second (not shown) bending modes of the plate. The associated natural frequency for the first bending mode is observed in the vicinity of 58 Hz and around 350 Hz for the second bending mode. With the information on the first two bending mode, we identify the material's Young's modulus and Poisson ratio by matching the predictions of the in vacuo structural mechanics model for the plate with the experimental determinations. Through this procedure, we estimate $E = 3.25 \times 10^9$ GPa, which is in line with typical polymeric materials [63], and v = 0.38, consistently with what found in similar materials [29, 54]. For ease of presentation, we assume a small constant structural damping with factor $\eta = 0.015$, so that the real Young's modulus for the structure is replaced by the complex version $E(1 + i\eta)$ in the calculations, see also [29, 54].

After the material identification is performed, a new set of experiments is performed in water, without removing the cantilever from its support, thereby avoiding to modify its boundary conditions and geometry. Room temperature water is used for the experiments, where we take $\rho_f = 9.9778 \times 10^2 \, \text{kg/m}^3$ and $\mu_f = 9.772 \times 10^{-4}$, Pa s. Underwater vibration experiments are performed in the frequency range between 0–85 Hz, similarly to what described above. Upon data postprocessing, we are able to identify the first two bending modes of the cantilever, at approximately 10.5 Hz ($f^+ = 0.68$) and 74 Hz ($f^+ = 4.8$). An underwater torsion mode is faintly detected in the neighborhood of 30.5 Hz ($f^+ \approx 2$), although experimental limitations cause some scatter in the data. It should also be noted that an ideal base excitation provides a symmetric load about the y-axis and theoretically should not excite antisymmetric modes such as the torsional ones. However, slight misalignments and other experimental uncertainties contribute to lightly excite that mode.

Without any further parameter tuning, we now calculate the FRF of the system by using our present nonlocal theory for cantilever plates. With the geometric and material properties presented above, the maximum value explored for the nondimensional frequency parameter is approximately $\beta = 1.4 \times 10^5$ and the mass ratio is $\mathcal{R} = 65.3$. Consistently with Eq. (6), the forcing vector is rewritten as

$$\hat{f}_{l}(\omega) = \hat{W}_{B}\omega^{2} \left[\int_{D} \rho_{s} h \Phi^{l}(\mathbf{x}) d\mathbf{x} + \frac{\hat{\Theta}_{B}}{\hat{W}_{B}} \int_{D} \rho_{s} h y \Phi^{l}(\mathbf{x}) d\mathbf{x} \omega^{2} \right] +$$

$$\hat{W}_{B} \left[\int_{D} \mathcal{H}_{\omega}[\mathbf{1}(\mathbf{x})] \Phi^{l}(\mathbf{x}) d\mathbf{x} + \frac{\hat{\Theta}_{B}}{\hat{W}_{B}} \int_{D} \mathcal{H}_{\omega}[y\mathbf{1}(\mathbf{x})] \Phi^{l}(\mathbf{x}) d\mathbf{x} \right]$$
(24)

Although we cannot measure the term $(\hat{\Theta}_B/\hat{W}_B)$ directly, we set it to a small real and positive value as to excite the asymmetric modes, to better illustrate the predictive capabilities of the nonlocal plate theory. Note that the first term on the right hand side of Eq. (24) describes the inertial load on the cantilever due to in vacuo vibrations, while the second term is the effect of the fluid. This last term is essential to construct the underwater FRF as its shape is determined by the complicated frequency dependence of the excitation.

Results of the present nonlocal plate theory are displayed in Fig. 15, which show the excellent agreement between our new model and the experimental results. Not only do the locations of the peaks coincide, but the model correctly captures the amplitude and shape of the response in the neighborhood of the peaks, further confirming the validity of our approach. For completeness, predictions of a beam-like local theory are displayed as well, demonstrating inadequacy of the local approach for low aspect ratio cantilevers. Remarkably, without any ad-hoc treatment,

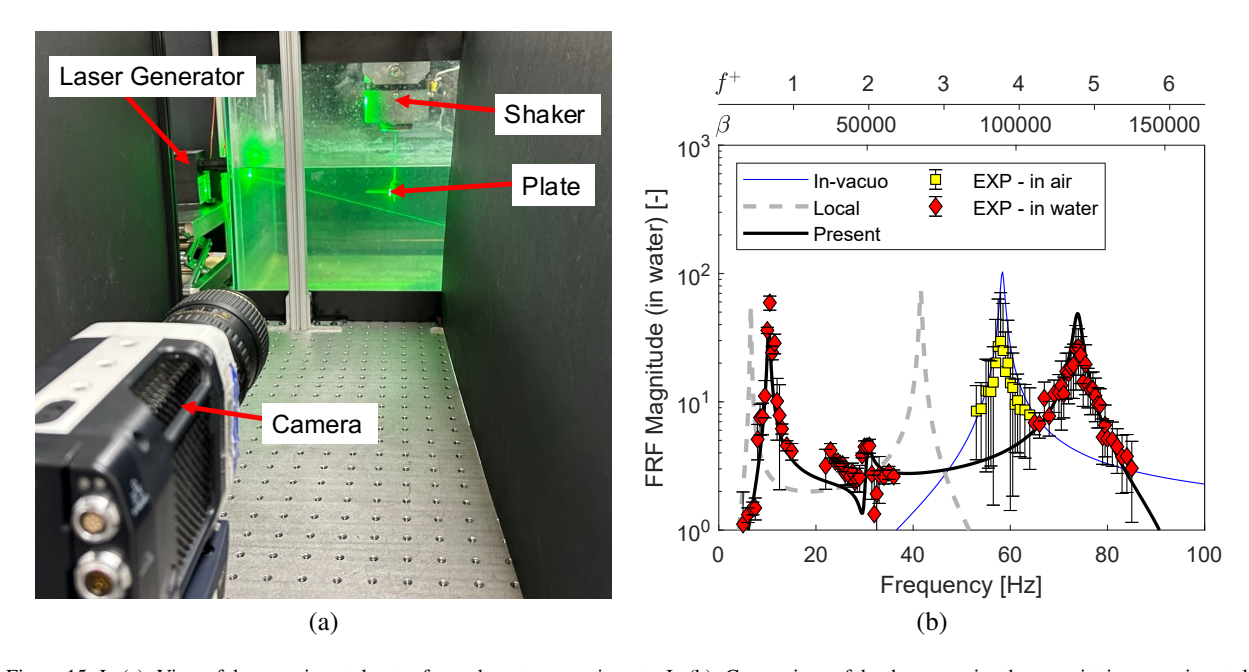


Figure 15: In (a): View of the experimental setup for underwater experiments. In (b): Comparison of the theory against base excitation experimental results. FRFs are presented with respect to dimensional frequency, as well as nondimensional parameters β and f^+ to emphasize hydrodynamic and structural regimes, respectively. Lines refer to the different theories: thin, in vacuo plate theory; dashed, beam-like underwater vibrations with local hydrodynamics treatment; thick, present nonlocal theory. Markers indicate experimental results: squares, in-air experiments; diamonds, underwater experiments. Error bars correspond to one standard deviation, as discussed in the text.

our plate theory correctly identifies the presence of the faint torsional mode. This is obviously not possible with a traditional local bending beam-like theory. Inspection of the nondimensional frequency scales in Fig. 15 demonstrate that the simple macroscale experiment we propose is completely consistent (from a "structural" perspective) with the microscale numerical studies, while the hydrodynamic regime is characterized by a relatively higher β range than those explicitly considered in the numerical studies. For this reason, genuinely microscale AFM-type experiments are currently under development to further explore the experimental implications of our theory in more viscous ranges. Results of these studies will be presented elsewhere.

We remark, in closing, that the discrepancies between the model and the experimental results are likely due to experimental limitations and uncertainties. Our primary challenges stem from optical constraints inherent in the large area of interest relative to the camera's field of view. This results in lower resolution, particularly impacting the precision in tracking the corners of the plate. Additional uncertainties in the experimental setup stem from possible misalignments between the laser sheet, the camera axis, and the plate, as well as from the uniform quality of illumination of the field of view. An additional experimental uncertainty is related to the temperature of the fluid, on which the parameter β depends weakly through the effect on density and viscosity. Furthermore, specific discrepancies in amplitude, localized in the neighborhood of the resonance peaks, can be possibly attributed to structural damping effects not pursued in this study (that could be accounted for with more accurate models for structural damping), and possible nonlinear effects in hydrodynamic damping at large vibration frequency and amplitudes (which could be corrected with ad hoc large amplitude numerical formulations, similar to [28, 29]). Specifically, note that in this experiment the maximum KC numbers are observed in proximity of the plate modes of vibration but never exceed 0.05. The corresponding maximum observed Reynolds number is of the order of β KC \approx 1200 at the second bending mode.

6. Conclusions

In this paper, we presented a nonlocal hydrodynamic theory for the study of cantilever beam and plate vibrations in an otherwise quiescent viscous fluid. The theory combines an efficient, low dimensional structural model derived

via a Rayleigh-Ritz method fully coupled with a nonlocal description of the hydrodynamic load as a function of the structural vibration. The hydrodynamic load is in turn derived by solving the fully 3D FSI problem via the unsteady Stokeslet method. Importantly, the solution of the otherwise computationally intensive fluid problem is conducted offline for prototypical plate vibrations with the purpose of constructing the novel nonlocal hydrodynamic function matrix. This matrix is the representation, in the basis formed by the structural modes, of the nonlocal hydrodynamic operator. Several new properties are highlighted for this construction, including the non-diagonal nature of the nonlocal hydrodynamic operator, its symmetry, and an interesting parity-preserving property. These are important departures from classical local hydrodynamic function formulations, and shed new light on the FSI problem, while also contributing useful numerical tools for its efficient treatment.

Once developed, we investigated our new theory implications on the treatment of cantilever vibrations in viscous fluids, demonstrating significant effects especially for flexible structures with low aspect ratios and high mode number, thus quantifying the inherent limitations of local theories which, by hypothesis, cannot properly address these instances. Among the major findings are the changes produced to the wet mode shapes by the presence of the fluid. Even for 1D solids (i.e., slender beams) all the dry modes are coupled and contribute to the vibration, as they are excited by the non-diagonal nature of the hydrodynamic operator. In addition, we demonstrated that the presence of the fluid causes significant dependence of the structural displacement field on the chord-wise direction. These findings demonstrate that a beam-like treatment, even if nonlocal, is largely incomplete and fails in capturing even relatively simple, or seemingly so, vibration scenarios.

We supported these conclusions by carefully addressing the peculiar behavior of frequency response functions for beams and plates, studying the effect of the diagonal and non-diagonal assumptions, quantitative properties of the dynamics, including quality factors and added mass coefficients, and highlighting significant differences stemming for low aspect ratios and high mode number. We reported on the differences between wet and dry modes, the difficulties arising in their tracking that led to the development of the concept of mode coherence, and the effect of the fluid on the structural response. Finally, we validated our novel theory against a new set of underwater experiments on the low-frequency vibrations of cantilever square plates under base excitation. These demonstrate that our novel theory can accurately predict, without any parameter tuning, the resonance frequencies of the wet modes, along with a seamless interpretation of the torsional response of the plate. Local beam theories, on the other hand, suffer from significant limitations in these determinations.

While this work presents a complete discussion of beams in bending and complex vibrations for plates, for clarity we decided not to include an ad hoc torsional theory of thin beams, due to a number of technical differences in the development. This theory will be presented elsewhere. Similarly, while our method is presented for an unbounded fluid, in principle it could be extended to bounded domains (including free surfaces or solid surfaces) and to the presence of multiple stationary or moving finite structures. In these contexts, of particular relevance in many sensing and actuation applications, the crucial contribution would be the proper modification of the hydrodynamic operator. A point of departure could be the extension of the boundary integral methods for solid surfaces in [25], for free surfaces in [26], and for arrays of solids in [64, 65]. Alternatively, the development of ad-hoc singularities as in [51, 3] could be pursued for reduced computational cost. We anticipate that for low aspect ratio structures, the departures from the results of local theories could be even more dramatic in the presence of bounding surfaces, due to the complexity of three dimensional flows. These lines of research will be explored in future works.

We remark here that the solution developed in this work is exact, up to: i) truncation errors in the modal expansion of the structural deformations; ii) discretization errors in the hydrodynamic problem; and iii) approximation errors inherent to the interpolations of functional values. In theory, all these errors can be rigorously removed from the formalism, although at the price of increased computational cost.

Appendix A. Mechanics of thin beams, in bending and torsion

In this section, we recall foundational aspects of the theory of vibrations of thin beams and provide the derivation of the structural matrices for use in the FSI problem. We describe separately the bending and the torsion problem.

Appendix A.1. Rayleigh-Ritz matrices for bending

We consider a thin Euler-Bernoulli beam, with uniform stiffness and mass properties, undergoing small bending deflections in the transverse direction. The beam axis, width, and thickness lie along x, y, and z axes of the reference

frame, respectively. The origin of the reference frame is placed at the centroid of the fixed-end cross section at x = 0. Length, width, and thickness of the beam are denoted as L, b, and h, respectively. The basic hypothesis is that the displacement field does not depend on the chord-wise coordinate y, so we will indicate it via w(x, t). The beam density (mass per unit volume) is indicated with ρ_s and its cross sectional area, uniform along the beam axis, is A = bh. The beam Young's modulus and Poisson's ratio are indicated with E and V, respectively, and the second area moment of inertia of the cross section with respect to the bending neutral axis is $I = bh^3/12$. The classical Euler-Bernoulli beam equations in the time domain can be found for example in [29] and are expressed as

$$EI\frac{\partial^4 w(x,t)}{\partial x^4} + \rho_s A \frac{\partial^2 w(x,t)}{\partial t^2} = f(x,t)$$
(A.1)

where f(x, t) represents a distributed load per unit length. We note here that often, especially in the case of wide beams (sometimes indicated as "plates in cylindrical bending"), the Young's modulus in plane strain may be used instead of E, indicated with $E' = E/(1 - v^2)$, see [66]. Typical cantilever (fixed-free) boundary conditions are given by

$$w(0,t) = 0; \frac{\partial w(x,t)}{\partial x}\Big|_{x=0} = 0; \frac{\partial^2 w(x,t)}{\partial x^2}\Big|_{x=L} = 0; \frac{\partial^3 w(x,t)}{\partial x^3}\Big|_{x=L} = 0$$
(A.2)

The potential elastic energy U and the kinetic energy T are given, respectively, by [52]

$$U = \frac{1}{2} \int_0^L EI\left(\frac{\partial^2 w(x,t)}{\partial x^2}\right)^2 dx; \ T = \frac{1}{2} \int_0^L \rho_s A\left(\frac{\partial w(x,t)}{\partial t}\right)^2 dx \tag{A.3}$$

We use, as assumed modes in a Rayleigh-Ritz method approach [39, 41], the dry modes of the fixed-free cantilever that can be written as, see [60],

$$\phi_i(x) = C_i \left[\sin(\lambda_i x/L) - \sinh(\lambda_i x/L) - \frac{\sin(\lambda_i) + \sinh(\lambda_i)}{\cos(\lambda_i) + \cosh(\lambda_i)} [\cos(\lambda_i x/L) - \cosh(\lambda_i x/L)] \right]$$
(A.4)

where λ_i is an eigenvalue obtained from the solution of the characteristic equation $\cos(\lambda_i)\cosh(\lambda_i)+1=0$ and C_i is a scaling constant, which is defined so that $\phi_i(L)=1$. Note that, for the first few dry mode shapes of the cantilever, λ_i are 1.8751041, 4.6940911, 7.8547574, 10.9955407, 14.1371684 and, correspondingly, C_i are 0.367048, -0.509234, 0.499612, -0.500017, 0.499999. We remark here that for relatively large mode order, the calculation of the eigenfunctions in Eq. (A.4) is numerically ill-conditioned because of the presence of hyperbolic functions. If i larger than approximately 10 is desired in double-precision calculations, the expression in Eq. (A.4) should be replaced with its asymptotic version provided in [67].

The dry modes of the cantilever satisfy all the homogeneous boundary conditions in Eq. (A.2). Using Hamilton's principle, and following standard procedures [52, 39], the Rayleigh-Ritz stiffness and mass matrix terms in Eq. (4) are expressed by

$$k_{ij} = \int_0^L EI\phi_{i,xx}(x)\phi_{j,xx}(x)dx; \ m_{ij} = \int_0^L \rho_s A\phi_i(x)\phi_j(x)dx$$
 (A.5)

where a subscript comma indicates derivative with respect to the indicated spatial variable. Note the symmetry of the mass and stiffness matrices, that is, $m_{ij} = m_{ji}$ and $k_{ij} = k_{ji}$. Similarly, the forcing term gives rise to a "modal" forcing vector, whose *i*-th component is given by $\int_0^L f(x,t)\phi_i(x)\mathrm{d}x$. Because of the orthogonality of the assumed modes chosen, the stiffness and mass matrices are actually diagonal, and their entries can be calculated analytically. The integration of the distributed load term can be performed numerically via Gauss-Legendre quadrature points [39]. Once the stiffness and mass matrices are determined, the solution of the eigenvalue problem $[K - \omega^2 M]q = 0$ provides the in vacuo natural flexural frequencies and mode shapes of the cantilever [60, 52]. For ease of presentation, we will also consider scaled versions, denoted with a superimposed tilde, of the stiffness and mass matrices, defined as $K = EIL\tilde{K}$ and $M = \rho_s AL\tilde{M}$. These forms help better highlight the role of fluid loading.

Appendix A.2. Rayleigh-Ritz matrices for torsion

The same beam is now subject to torsional vibrations along its axis x. We will not use here a plate formalism, but the classical treatment of torsion for rectangular thin cross section beams. The same treatment was also proposed in [24, 54]. The basic hypothesis is that the displacement field can be described uniquely by the twist angle $\theta(x, t)$, via the relation $w(x, y, t) = y\theta(x, t)$. Relevant static and stiffness property for the cross section are the moment of inertia $I_t = b^3 h/12$ and the torsional stiffness GJ_t where G = E/(2(1 + v)) is the shear modulus and $J_t = bh^3/3$ a geometric section property. Under the usual simplified description for thin rectangular cross sections, the twist angle $\theta(x, t)$ obeys the following wave equation in the time domain, see for example [54]

$$GJ_t \frac{\partial^2 \theta(x,t)}{\partial x^2} - \rho_s I_t \frac{\partial^2 \theta(x,t)}{\partial t^2} = m_t(x,t)$$
(A.6)

where $m_t(x,t)$ represents a distributed moment (torque) per unit length. Typical cantilever (fixed-free) boundary conditions are given by

$$\theta(0,t) = 0; \frac{\partial \theta(x,t)}{\partial x}\Big|_{x=L} = 0$$
 (A.7)

The potential elastic energy U and the kinetic energy T and are given, respectively, by

$$U = \frac{1}{2} \int_0^L G J_t \left(\frac{\partial \theta(x, t)}{\partial x} \right)^2 dx; \ T = \frac{1}{2} \int_0^L \rho_s I_t \left(\frac{\partial \theta(x, t)}{\partial t} \right)^2 dx \tag{A.8}$$

We use as assumed modes for the twist angle the dry modes of a fixed-free rod under torsion, that is, see [60],

$$\phi_i^t(x) = \sin(\lambda_i x/L) \tag{A.9}$$

where the superscript t stands for torsion, and λ_i is an eigenvalue obtained from the solution of the characteristic equation $\cos(\lambda_i) = 0$, that is, $\lambda = (2i - 1)\pi/2$. Using Hamilton's principle, the Rayleigh-Ritz stiffness and mass matrix terms in Eq. (4) are expressed by

$$k_{ij} = \int_0^L G J_t \phi_{i,x}^t(x) \phi_{j,x}^t(x) dx; \ m_{ij} = \int_0^L \rho_s I_t \phi_i^t(x) \phi_j^t(x) dx$$
 (A.10)

Note the symmetry of the mass and stiffness matrices, that is, $m_{ij} = m_{ji}$ and $k_{ij} = k_{ji}$. Similarly, the forcing term gives rise to a "modal" forcing vector, whose *i*-th component is given by $\int_0^L m_t(x,t)\phi_i^t(x)dx$. Because of the orthogonality of the assumed modes chosen, the stiffness and mass matrices are actually diagonal, and their entries can be calculated analytically. As above, the integration of the distributed load term can be performed numerically via Gauss-Legendre quadrature points [39]. Once the stiffness and mass matrices are determined, the solution of the eigenvalue problem $[K - \omega^2 M]q = 0$ provides the in vacuo natural torsional frequencies and mode shapes of the cantilever beam [60, 52]. As before, we will also consider scaled versions, denoted with a superimposed tilde, of the stiffness and mass matrices, defined as $K = GJ_tL\tilde{K}$ and $M = \rho_s I_tL\tilde{M}$. It is important to remark here that the modal coefficients in q describe the twist angle so that, if we want to recover the displacements of the plate, we set $w(x, y, t) = y \sum_i q_i(t)\phi_i^t(x)$. Results from the torsional theory for beams are compared with predictions from the nonlocal plate theory developed in this work. A nonlocal theory for torsional vibrations of beams will be reported elsewhere for clarity of presentation.

Appendix B. Mechanics of classical thin plates

In this section, we recall foundational aspects of the theory of vibrations of thin plate and provide the derivation of the structural matrices for use in the FSI problem.

We consider a thin Kirchhoff-Love plate, with uniform stiffness and mass properties, undergoing small deflections in the transverse direction. The undeformed plate mid-plane lies in the xy-plane, and its length, width, and thickness lie along the x, y, and z axes of the reference frame, respectively. The origin of the reference frame is placed at the centroid of the fixed-end cross section at x = 0. Length, width, and thickness of the plate are denoted as L, b, and h, respectively. The fixed edge is at x = 0, and the free edges are at x = L and $y = \pm b/2$. The plate density (mass per

unit volume) is indicated with ρ_s . Material properties include Young's modulus E and Poisson's ratio ν . The classical Kirchoff-Love plate equations in the time domain for the displacement field w(x, y, t) can be found for example in [66] and are expressed, by neglecting membrane behavior, as

$$D\nabla^4 w(x, y, t) + \rho_s h \frac{\partial^2 w(x, y, t)}{\partial t^2} = f(x, y, t)$$
(B.1)

where f(x, y, t) represents a distributed load per unit area, $D = Eh^3/[12(1 - v^2)]$ is the plate flexural rigidity, and ∇^4 is the bilaplacian operator, that is, $\nabla^4 w = w_{,xxxx} + 2w_{,xxyy} + w_{,yyyy}$. Note that Eq. (A.1) can be recovered from Eq. (B.1) by neglecting all dependence on the y coordinate, setting to 0 each derivative with respect to y, integrating over $y \in (-b/2, b/2)$, and replacing the Young's modulus in Eq. (A.1) with E'. Vice versa, Eq. (A.6) cannot be obtained directly from Eq. (B.1), because the underlying hypotheses are different.

For the plate problem, typical cantilever (fixed-free-free) boundary conditions are given by

$$w = 0$$
 and $w_{,x} = 0$ at $x = 0$
 $w_{,xxx} + (2 - v)w_{,xyy} = 0$ and $w_{,xx} + vw_{,yy} = 0$ at $x = L$
 $w_{,yyy} + (2 - v)w_{,yxx} = 0$ and $w_{,yy} + vw_{,xx} = 0$ at $y = \pm b/2$ (B.2)

If a Galerkin approach were to be used in the derivation of the structural matrices, a complete set of basis functions that satisfies all the boundary conditions in (B.2) should be employed. A natural choice would be the dry plate modes, which however are not known exactly in the general case. Alternatively, we could select a set of basis functions that do not satisfy the boundary conditions, but then boundary terms would need to be added to formulation of the matrices [53].

A more practical approach is the use of Rayleigh-Ritz method, from the expressions of the potential and kinetic energy of the plate. The potential elastic energy U and the kinetic energy T are given, respectively, by [41, 39, 52]

$$U = \frac{1}{2} \int_{-b/2}^{b/2} \int_{0}^{L} D\left[(w_{,xx})^{2} + (w_{,yy})^{2} + 2\nu w_{,xx} w_{,yy} + 2(1 - \nu)(w_{,xy})^{2} \right] dxdy$$

$$T = \frac{1}{2} \int_{-b/2}^{b/2} \int_{0}^{L} \rho_{s} h \left(\frac{\partial w(x,t)}{\partial t} \right)^{2} dxdy$$
(B.3)

We then use, as the assumed modes, separable functions obtained as the product of the dry modes of a fixed-free cantilever in the *x*-direction, that is, the $\phi_i(x)$ above in Eq. (A.4), and of a free-free cantilever [60] in the *y*-direction, that we indicate with $\varphi_i(y)$. These are $\varphi_0(y) = 1$, describing the cross sectional translational rigid body mode (for plate cylindrical bending), $\varphi_1(y) = 2y/b$, describing the cross sectional rotational rigid body mode (for plate torsion), and

$$\varphi_i(\bar{y}) = C_i \left[\sin(\lambda_i \bar{y}/b) + \sinh(\lambda_i \bar{y}/b) - \frac{\sin(\lambda_i) - \sinh(\lambda_i)}{\cos(\lambda_i) - \cosh(\lambda_i)} [\cos(\lambda_i \bar{y}/b) + \cosh(\lambda_i \bar{y}/b)] \right]$$
(B.4)

for $i \ge 2$, with $\bar{y} = y + b/2$, for notational convenience. The eigenvalues λ satisfy the characteristic equation $\cos(\lambda_i) \cosh(\lambda_i) - 1 = 0$ and, besides the double root $\lambda_0 = \lambda_1 = 0$ their first few values (for $i \ge 2$) are 4.7300407, 7.8532046, 10.9956078, 14.1371655. The corresponding first few scaling coefficients C_i are given by -2.035619, 1.998447, -2.000067, 1.999997. Here again, for relatively large mode order, the calculation of the eigenfunctions in Eq. (B.4) is numerically ill-conditioned because of the presence of hyperbolic functions. If i larger than approximately 10 is desired in double-precision calculations, the expression in Eq. (B.4) should be replaced with its asymptotic version provided in [67].

The assumed modes of the cantilever plate are then given by $\Phi^I(x,y) = \phi_i(x)\varphi_j(y)$, provided that a suitable numbering convention is adopted that maps the pair of indices (i,j) to the index I. One such possible ordering, that does not use information on the maximum number of modes used for the expansion, could be given by I = (i+j-1)(i+j)/2 + (j+1). The ordering is similar to Cantor's enumeration or diagonal traversing of the entries of a matrix and, for example, the mode with i=3, j=1 would be uniquely identified with the index I=8. In general, however, this ordering does not ensure that the modes are sorted by increasing natural frequency, although this does

not cause any issues. While the numbering convention is used in the calculations, we often refer to mode (i, j) to indicate the plate mode $\phi_i(x)\varphi_j(y)$ for clarity of exposition.

Using Hamilton's principle, and following standard procedures [39], the Rayleigh-Ritz stiffness and mass matrix terms in Eq. (4) are expressed by

$$k_{IJ} = \int_{-b/2}^{b/2} \int_{0}^{L} D\left[\Phi_{,xx}^{I} \Phi_{,xx}^{J} + \Phi_{,yy}^{I} \Phi_{,yy}^{J} + \nu(\Phi_{,xx}^{I} \Phi_{,yy}^{J} + \Phi_{,yy}^{I} \Phi_{,xx}^{J}) + 2(1-\nu)\Phi_{,xy}^{I} \Phi_{,xy}^{J}\right] dxdy$$

$$m_{IJ} = \int_{-b/2}^{b/2} \int_{0}^{L} \rho_{s} h \Phi^{I} \Phi^{J} dxdy$$
(B.5)

Note the symmetry of the mass and stiffness matrices. Similarly, the forcing term gives rise to a "modal" forcing vector, whose *I*-th component is given in the time domain by $\int_{-b/2}^{b/2} \int_{0}^{L} f(x,y,t) \Phi^{I}(x,y) dxdy$. The double integrals of this section are performed numerically via Gauss-Legendre quadrature points, see [39] where relevant computational details can be found, although therein Legendre polynomials are used for the modes in the *y*-direction. It should be noted that the choice of assumed modes in the Rayleigh-Ritz method is arbitrary, provided that the modes form a complete basis and satisfy the essential boundary conditions of the problem, see also [52]. Once the stiffness and mass matrices are determined via numerical integration, the solution of the eigenvalue problem $[K - \omega^2 M]q = 0$ provides the in vacuo natural frequencies and mode shapes of the cantilever plate [60, 52]. These will include cylindrical (beamlike) bending modes, torsional modes, and proper plate-like modes. As above, we will also consider scaled versions, denoted with a superimposed tilde, of the stiffness and mass matrices, defined as $K = DLb\tilde{K}$ and $M = \rho_s hLb\tilde{M}$. These forms help better highlight the role of fluid loading.

Although not pursued in depth in this paper, the mechanics models can be easily extended to orthotropic plates, that are often of interest in the analysis of crystalline silicon-based microsystems [68, 35]. In this case, we assume the elastic properties to be constant in the through-the-thickness direction, and we indicate with c_{ij} the components in Voigt notation of the material's elastic tensor, such that the stresses σ_{ij} are related to the strains ϵ_{kl} via $\sigma_{ij} = C_{ijkl}\epsilon_{kl}$. We have $c_{11} = C_{1111} = E_x/(1 - v_{xy}v_{yx})$; $c_{22} = C_{2222} = E_y/(1 - v_{xy}v_{yx})$; $c_{12} = C_{1122} = v_{xy}c_{22} = v_{yx}c_{11}$; and $c_{66} = C_{1212} = G_{xy}$. As usual, E_x and E_y indicate the Young's moduli in the x- and y-direction, respectively, G_{xy} is the shear modulus in the xy-plane, and the Poisson ratios v_{ij} describe a contraction in the j-direction when extension is applied in the i-direction; note also that $v_{ij} = v_{ji}(E_j/E_i)$, see [69]. As customary, by denoting with $D_{ij} = \int_{-b/2}^{b/2} c_{ij}z^2 dz$ the stiffness moduli of the plate, Eq. (B.1) is replaced by [70, 66]

$$\left[D_{11}\frac{\partial^4}{\partial x^4} + 2(D_{12} + 2D_{66})\frac{\partial^4}{\partial x^2 \partial y^2} + D_{22}\frac{\partial^4}{\partial y^4}\right]w(x, y, t) + \rho_s h \frac{\partial^2 w(x, y, t)}{\partial t^2} = f(x, y, t)$$
(B.6)

Similarly, we replace the expression for the elastic energy U in Eq. (A.3) with [70, 52]

$$U = \frac{1}{2} \int_{-b/2}^{b/2} \int_{0}^{L} \left[D_{11}(w_{,xx})^{2} + D_{22}(w_{,yy})^{2} + 2D_{12}w_{,xx}w_{,yy} + 4D_{66}(w_{,xy})^{2} \right] dxdy$$
 (B.7)

The orthotropic plate stiffness matrix can be calculated by following the same procedure as above. We obtain

$$k_{IJ} = \int_{-b/2}^{b/2} \int_{0}^{L} \left[D_{11} \Phi_{,xx}^{I} \Phi_{,xx}^{J} + D_{22} \Phi_{,yy}^{I} \Phi_{,yy}^{J} + D_{12} (\Phi_{,xx}^{I} \Phi_{,yy}^{J} + \Phi_{,yy}^{I} \Phi_{,xx}^{J}) + 4D_{66} \Phi_{,xy}^{I} \Phi_{,xy}^{J} \right] dxdy$$
 (B.8)

Appendix B.1. Numerical validation of the mechanical model

The mechanical model is validated for numerical accuracy against results from a commercial finite element method (FEM) solver. In this section, we report a representative case for an isotropic and an orthotropic microplate, inspired by the systems discussed in [35, 68]. For the isotropic case, we consider a silicon microplate with $L = 500 \,\mu\text{m}$, $b = 250 \,\mu\text{m}$, and $h = 10 \,\mu\text{m}$, with $\rho_s = 2330 \,\text{kg/m}^3$, $E = 169 \,\text{GPa}$, v = 0.25. In our Rayleigh-Ritz model, we use 10 modes in the x-direction and 10 modes in the y-direction. We use 41 Gauss-Legendre quadrature points in both the x- and y-direction to accurately evaluate the integrals in Eq. (B.5). For the orthotropic case, we use the same plate geometry, as well as the same numerical details for the integration, while we adopt the following material coefficients

from [68]: $E_x = E_y = 169 \,\text{GPa}$, $E_z = 130 \,\text{GPa}$, $v_{yz} = 0.36$, $v_{zx} = 0.28$, $v_{xy} = 0.064$, $G_{yz} = G_{zx} = 79.6 \,\text{GPa}$, $G_{xy} = 50.9 \,\text{GPa}$. This leads to elastic tensor coefficients approximately equal to $c_{11} = c_{22} = 169.7 \,\text{GPa}$, $c_{12} = 10.86 \,\text{GPa}$, and $c_{66} = 50.9 \,\text{GPa}$. Incidentally, there appears to be some typos in the matrix in Eq. (8) of Ref. [68] where the c_{ij} coefficients are reported.

Finite element simulations are conducted in the commercial software package ANSYS Mechanical APDL 17.0, and are similar to the setup discussed in [39]. Briefly, the plate is modeled as a 2D solid and shell elements are used in the simulation, with only bending (and no membrane) stiffness consistently with our strain energy formulations in Eq. (B.3). Also, to closely approximate the hypothesis of our mechanical model, we suppress out of plane displacements and neglect rotational degrees of freedom in the element technology. For this elementary problem, the rectangular plate is meshed with 5000 mapped square elements of $5\,\mu\rm m$ side. The first few modes are resolved via a modal analysis in the software which uses block Lanczos methods for the eigenvalue problem, whose size is 15300 equations. For comparison, our Rayleigh-Ritz model only contains 100 equations. Results of the modal analysis are presented in Table B.2, where the first 10 natural frequencies of the systems are expressed in kilohertz. In every case, our mechanical model recovers FEM results with less than 0.3% relative error. This validates the Rayleigh-Ritz method presented in this appendix for the mechanical problem.

Table B.2: Verification of the mechanical model for isotropic and orthotropic plate against results from FEM results. Resonance frequencies for the first ten modes of the plate are expressed in kilohertz.

	Iso	tropic Silico	n	Orthotropic Silicon				
Mode	Present	FEM	% error	Present	FEM	% error		
1	56.160	55.994	0.296	55.099	55.088	0.021		
2	246.583	246.414	0.069	217.568	217.530	0.017		
3	350.607	349.589	0.290	345.216	345.162	0.016		
4	799.708	798.640	0.133	714.341	714.070	0.038		
5	983.385	980.685	0.275	966.681	966.678	0.000		
6	1517.542	1513.750	0.250	1393.222	1392.950	0.020		
7	1528.167	1525.130	0.199	1462.241	1461.950	0.020		
8	1933.988	1929.700	0.222	1884.026	1883.900	0.007		
9	2074.021	2070.940	0.149	1904.363	1904.400	-0.002		
10	2513.833	2507.830	0.239	2335.088	2335.290	-0.009		

Appendix C. Further details on the fluid problem

Appendix C.1. Oscillatory Stokelets for 3D flow field calculations

Equation (8) can be used to reconstruct the full 3D velocity field of the fluid in response to a net traction $[[\tau]](x)$ on the plate. The full expressions for the kernels S_{13} , S_{23} , and S_{33} for calculation of the fluid velocities in the x, y, and z directions, respectively, are adapted from [51] and, with the nomenclature of this paper, are

$$S_{i3} = A(R)\frac{\delta_{i3}}{r} + B(R)\frac{r_i r_3}{r^3}$$
 (C.1)

Here, δ_{ij} is the Kronecker delta, $\mathbf{r} = \mathbf{x} - \bar{\mathbf{x}}$ indicates the vector between one point \mathbf{x} on the cantilever and one point $\bar{\mathbf{x}}$ in the fluid domain, r_i are its components, and $r = |\mathbf{r}|$ its magnitude. In addition, $R = \sqrt{i}\alpha r$ and

$$A(R) = 2e^{-R}(1 + 1/R + 1/R^2) - 2/R^2; \quad B(R) = -2e^{-R}(1 + 3/R + 3/R^2) + 6/R^2$$
 (C.2)

By calculating the curl of the velocity vector, we can also use our BEM approach to determine the vorticity vector in the flow field by evaluating

$$\hat{\zeta}_{i}(\mathbf{x}) = \varepsilon_{ijk} \frac{\partial}{\partial \bar{x}_{i}} \hat{u}_{k}(\bar{\mathbf{x}}) = \frac{1}{8\pi} \int_{\mathbf{D}} [[\hat{\tau}]](\mathbf{x}) \varepsilon_{ijk} \frac{\partial S_{k3}(\mathbf{x}, \bar{\mathbf{x}}; \alpha)}{\partial \bar{x}_{i}} \, d\mathbf{x} = \frac{1}{8\pi} \int_{\mathbf{D}} [[\hat{\tau}]](\mathbf{x}) \Omega_{i3}(\mathbf{x}, \bar{\mathbf{x}}; \alpha) \, d\mathbf{x}$$
(C.3)

with ε_{kji} the Levi-Civita symbol and

$$\Omega_{i3} = 2\varepsilon_{i3\ell}(r_{\ell}/r^3)e^{-R}(R+1)$$
(C.4)

is the oscillatory rotlet [51]. Note, in particular, that $\hat{\zeta}_3 = 0$, as expected. More in general, the spatial derivative of the velocity $\partial \hat{u}_i/\partial \bar{x}_i$ can be calculated via the kernel

$$\frac{\partial S_{i3}(\boldsymbol{x}, \bar{\boldsymbol{x}}; \alpha)}{\partial \bar{x}_i} = C(R) \frac{r_j \delta_{i3}}{r^3} + D(R) \frac{r_i r_j r_3}{r^5} - B(R) \frac{(r_i \delta_{3j} + r_3 \delta_{ij})}{r^3}$$
(C.5)

with

$$C(R) = A(R) - R \frac{\partial A(R)}{\partial R} = 2e^{-R} (3/R^2 + 3/R + 2 + R) - 6/R^2$$

$$D(R) = 3B(R) - R \frac{\partial B(R)}{\partial R} = 30/R^2 - 2e^{-R} (15/R^2 + 15/R + 6 + R)$$
(C.6)

Representative 3D flow fields obtained with the unsteady singularities above are reported in the main text for selected shapes at wet resonance of the vibrating plate.

Appendix C.2. Remarks on numerical aspects of the fluid problem

Using the scaling proposed in Eq. (16), the governing parameters of the hydrodynamic problem are the aspect ratio Λ and the frequency parameter β . Without lack of generality, in our numerical solution to the integral equation in Eq. (9) and successive calculation of $\tilde{h}_{ij}(\beta)$, we explore the space of parameters by first letting unit width b=1 m, and $\rho_f=998.2$ kg m⁻³ and $\mu_f=1.003\times 10^{-3}$ Pa s for liquid water at room temperature. The dimensional frequency ω and cantilever length L are selected as to provide values in the range $\beta\in[10^0,10^6]$ and $\Lambda\in[1,20]$, respectively, so as to explore the limits of very viscous to essentially inviscid behavior, for slender beams to square plates geometries. A discussion of the asymptotic treatment of the hydrodynamic problem for very low to moderate nondimensional frequencies can be found in Appendix D.

The numerical solution of the integral equation in Eq. (9) is obtained by discretizing the surface of the cantilever into progressively finer meshes of 8×8 , 16×16 , 32×32 , and 64×64 panels, with trigonometric refinement towards the edges, following our previous work [46]. The trigonometric refinement ensures progressively smaller panel sizes as one approaches the edges, and has unique singularity-handling capabilities as discussed for example in [22]. This is particularly important when dealing with the singular velocity and pressure behavior on the solid surface sharp edges. Examples of a typical mesh is shown in Fig. 1. Results are found to be essentially indistinguishable between the 32×32 mesh and the 64×64 mesh, especially for moderately large values of β . Thus, the 64×64 mesh is used everywhere in this study.

For each combination of aspect ratio and frequency desired, in the numerical solution, the unknown $[[\hat{\tau}]]$ is assumed to be piecewise constant on each mesh panel, and the resulting discrete boundary element problem is solved as in [46]. Specifically, \bar{x} is evaluated at the center of each panel, and integrals of $\mathcal{A}(|x-\bar{x}|,\alpha)$ are evaluated numerically with the adaptive 2D quadrature method in the subroutine quad2d in the software package MathWorks MATLAB. We remark that, when constructing the system matrices, if x and \bar{x} belong to different panels (off-diagonal terms), the integrand is well-behaved and the numerical integration is trivial. On the other hand, in the calculation of diagonal terms in the system matrices, the singularity in \mathcal{A} as $x = \bar{x}$ must be carefully accounted for, by following for example the procedure in [46], which relies on explicit integration of the singularity. System matrices are constructed for each combination of aspect ratio and nondimensional frequency and are inverted once and for all (and, in fact, stored in factored form) before the calculation of $[[\hat{\tau}]]$ for a given left-hand side in Eq. (9). Representative calculations of the net hydrodynamic traction profiles corresponding to prescribed velocity profiles are shown in Fig. 2. After the $\tilde{h}_{ij}(\beta)$ terms are calculated, Eq. (16) is used to determine the dimensional values to include in structural dynamics equations.

The last detail necessary for the determination of the modal hydrodynamic forces lies in the treatment of possible values of β and Λ that may appear in the structural dynamic equations but have not been explicitly calculated with the procedure discussed above. In fact, the operator $H(\omega)$ in Eq. (5) should be interpreted as a function of the real-valued variable ω , while only a finite set of values of ω (or, equivalently, β) are used in the determination of the modal hydrodynamic function. Similarly, it is not practical to simulate all aspect ratios of interest, as a new set of matrices has to be constructed, with possibly significant computational cost. To obviate this computational limitation, we construct interpolation tables from the available 2D space in (β, Λ) . Specifically, a first interpolation is performed as a function of Λ to determine the operator $H(\omega)$ at a set of discrete β points for a desired aspect ratio. Finally, a second

interpolation as a function of β is used for the estimation of modal hydrodynamic forces at desired frequencies to be used in structural dynamics calculations. This approach is robust and computationally inexpensive and conducted in the software package MathWorks MATLAB using the subroutine interp1 with option makima. An alternative approach to the interpolation could be the identification of suitable fit functions for the real and imaginary parts of all the entries of the matrix $H(\omega)$, similar to those presented in [29]. This could also be extended to the different aspect ratios. However, in this paper, we will not pursue this avenue, as the added complexity of developing extensive look up tables of numerical coefficients does not result in improved theoretical or numerical understanding of the problem.

Appendix D. Low frequency asymptotic behavior

In this section, we develop an asymptotic theory for the nonlocal modal hydrodynamic function matrix that is valid in the limit of low frequency behavior. This dynamic range rigorously incorporates the steady Stokes regime, where fluid forces are proportional to velocities (and the hydrodynamic functions are purely imaginary), and extends to a "quasi-steady" regime, where the forces are expressible in powers of the frequency.

Our point of departure are Eqs. (9) and (10). We use a perturbation solution scheme for the Fredholm integral equation in Eq. (9) similar to the one discussed in [71]. Since in the steady Stokes regime $\alpha \to 0$, we first consider a series expansion of the kernel $\mathcal{A}(r,\alpha)$ about $\alpha=0$. This yields

$$\mathcal{A}(r,\alpha) = \frac{1}{r} - \frac{4(1+i)}{3\sqrt{2}}\alpha + \frac{3}{4}ir\alpha^2 + O(\alpha^3)$$
 (D.1)

The zero-th order term of the expansion, $\mathcal{A}_0(r) = 1/r$, is the (3,3) component of the Oseen tensor localized on the plate surface, see also [51], while the first order term of the expansion $-\mathcal{A}_1\alpha$, with \mathcal{A}_1 a complex constant, can be considered as a perturbation of the tensor describing the steady Stokes regime. We retain up to the second order expansion, $\alpha^2 \mathcal{A}_2$, for a reason that will become clear later. Note that this last term is purely imaginary and scales with r.

We postulate that the hydrodynamic stresses on the plate can also be expressed in a power series of α so that $[[\hat{\tau}]] = [[\hat{\tau}]]_0 + \alpha[[\hat{\tau}]]_1 + \alpha[[\hat{\tau}]]_2 + O(\alpha^3)$. Upon substituting these expressions in Eq. (9), neglecting higher order terms in α , and indicating the phasor of the transverse (nondimensional) velocity of the plate with $i\hat{w}/b$, we obtain

$$i\hat{w}(\bar{\mathbf{x}})/b = \frac{1}{8\pi} \int_{D} \left([[\hat{\tau}]]_{0}(\mathbf{x}) + \alpha[[\hat{\tau}]]_{1}(\mathbf{x}) + \alpha^{2}[[\hat{\tau}]]_{2}(\mathbf{x}) \right) \left(\mathcal{A}_{0}(|\mathbf{x} - \bar{\mathbf{x}}|) - \alpha \mathcal{A}_{1} + \alpha^{2} \mathcal{A}_{2}(|\mathbf{x} - \bar{\mathbf{x}}|) \right) d\mathbf{x}$$
(D.2)

Note that \hat{w} is here considered of order $O(\alpha^0)$ without loss of generality, as Eq. (D.2) is linear. Equating powers of α and neglecting terms of order $O(\alpha^3)$, Eq. (D.2) leads to the following three integral equations

$$\int_{D} [[\hat{\tau}]]_{0}(\mathbf{x}) \mathcal{A}_{0}(|\mathbf{x} - \bar{\mathbf{x}}|) d\mathbf{x} = i8\pi \hat{w}(\bar{\mathbf{x}})/b$$
(D.3)

$$\int_{D} [[\hat{\tau}]]_1(\mathbf{x}) \mathcal{A}_0(|\mathbf{x} - \bar{\mathbf{x}}|) d\mathbf{x} = \mathcal{A}_1 \int_{D} [[\hat{\tau}]]_0(\mathbf{x}) d\mathbf{x}$$
 (D.4)

$$\int_{D} [[\hat{\tau}]]_{2}(x) \mathcal{A}_{0}(|x - \bar{x}|) dx = \mathcal{A}_{1} \int_{D} [[\hat{\tau}]]_{1}(x) dx - \int_{D} [[\hat{\tau}]]_{0}(x) \mathcal{A}_{2}(|x - \bar{x}|) dx$$
 (D.5)

which must be solved sequentially for $[[\hat{\tau}]]_0$ from Eq. (D.3), $[[\hat{\tau}]]_1$ from Eq. (D.4), and $[[\hat{\tau}]]_2$ from Eq. (D.5). Interestingly, the same kernel 1/r appears in the left hand side of all the integral equations above. Therefore, solution of the stress distributions only involves the construction and inversion of a single real-valued matrix, for a given plate aspect ratio. This task can be approached with the same methods described in Appendix C.2. We remark that, also in this case, in the calculation of diagonal terms in the system matrices, the singularity 1/r in the kernel must be carefully handled by explicit (although trivial) integration.

A few comments, stemming from the analytical structure of Eqs. (D.3), (D.4), and (D.5), are in order. At the zero-th order, because the kernel \mathcal{A}_0 is real, the hydrodynamic stresses $[[\hat{\tau}]]_0$ are imaginary, and thus, in phase with the velocities, consistently with the notion of steady Stokes flow [72]. These stresses, therefore, contribute only to hydrodynamic damping. At the first order, we observe that the right hand side of Eq. (D.4) is a constant, for any value

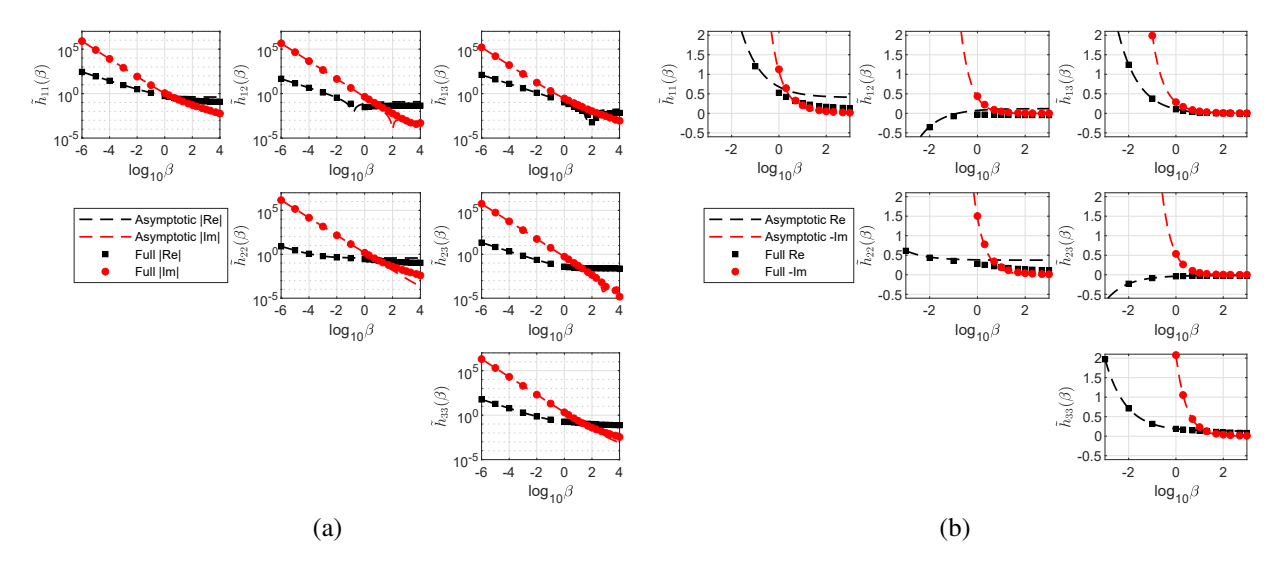


Figure D.16: Representative components of the hydrodynamic function matrix \tilde{H} (markers) for aspect ratio $\Lambda = 1$, along with the asymptotic scaling laws (dashed lines) showing the components of \tilde{H}^A in the basis of the cantilever beam modes. In (a): log-log plot of the asymptotic behavior with emphasis over the low frequency range. In (b): semilog plot comparison of the asymptotic formula in an intermediate frequency range.

of \bar{x} . Furthermore, the real and imaginary part of this constant are numerically equal. This means that the solution of the hydrodynamic stresses $[[\hat{\tau}]]_1$ will be a complex-valued vector, whose real and imaginary part are equal. Therefore, at the first order in α , the hydrodynamic forces will include an added mass effect and a hydrodynamic damping effect which are numerically equivalent. Finally, it can be easily shown that, at the second order, the right hand side of Eq. (D.5) is purely real, thus leading to a real-valued fluid force in quadrature with the velocity, that is, an added mass.

We can now proceed to the definition of the asymptotic modal hydrodynamic function matrix. Similar to the development of Eq. (14), we denote with $\hat{\chi}_{\phi_j|0}$, $\hat{\chi}_{\phi_j|1}$, and $\hat{\chi}_{\phi_j|2}$ the zero-th, first, and second order solutions, respectively, of Eqs. (D.3), (D.4), and (D.5) when the velocity is prescribed to the *j*-th mode shape, that is, $i\phi_j(x)$

$$h_{ij}^{A}(\omega) = \mu_f \omega \int_{\mathbf{D}} \phi_i(\mathbf{x}) [\hat{\chi}_{\phi_j|0}(\mathbf{x}, \omega) + \alpha \hat{\chi}_{\phi_j|1}(\mathbf{x}, \omega) + \alpha^2 \hat{\chi}_{\phi_j|2}(\mathbf{x}, \omega)] d\mathbf{x}$$
 (D.6)

where the superscript A indicates the asymptotic form. Scaling this expression consistently with Eq. (16), we thus divide by the term $(\pi/4)\rho_f\omega^2b^2L$, leaving an ω term in the denominator of h_{ij}^A . Recalling that ω is proportional to β and α is proportional to $\sqrt{\beta}$, we obtain for the asymptotic hydrodynamic function matrix the following form

$$\tilde{\mathbf{H}}^{A}(\beta) = i\beta^{-1}N_0 + (1+i)\beta^{-1/2}N_1 + N_2 \tag{D.7}$$

where N_0 , N_1 , and N_2 are real-valued, constant matrices that depend only on the aspect ratio of the plate (once the modal basis is prescribed). A physical interpretation of the powers in Eq. (D.7), which are consistent with the classical development of unsteady boundary layer theory [73, 47, 74] (although derived for large β) and generalize the local asymptotic results in [1] or the semi-empirical results in [29], stems from the observation that $\tilde{H}^A(\beta)$ would multiply an acceleration-like term in Eq. (18). The power β^{-1} thus describe an integrator, and therefore a damping term proportional to velocity (steady Stokes forces). The power $\beta^{-1/2}$ is instead a Basset-like "history" term, as a multiplication by a $1/\sqrt{\pi t}$ in the frequency domain corresponds to a convolution with a term $1/\sqrt{\pi t}$ in the time domain. Finally, the constant term represents a component in phase with the acceleration, that is, an added mass term.

This expression provides the desired asymptotic representation for the modal hydrodynamic function matrix and is depicted for illustration in Fig. D.16 for unit aspect ratio. This particular figure reproduces the data discussed in Fig. 4(b), although replotted in an extended window to the very low β range to illustrate the asymptotic behavior. Note that in the asymptotic analysis, the perturbation parameter is $\alpha \sim \sqrt{\beta}$; thus, the validity of the asymptotic approximation is expected only for low values of β . It should be noted that, as opposed to Fig. 4, the data are reported on a

log-log scale in Fig D.16(a), so as to better display the scaling laws at low frequency. Because of the presence of positive and negative values, we decide to report the absolute values of the real and imaginary parts of the hydrodynamic function; to this choice is also due the presence of peculiar "dips" in the data, which likely identify a zero-crossing point in the data and the asymptotic expressions. The asymptotic behavior is reported in Fig D.16(b) in semilog scale to accentuate the small values of the hydrodynamic functions at high frequency. As expected, discrepancies seem more pronounced in the relatively large β range, where the asymptotic expression becomes inaccurate; however, all the trends of the data are correctly captured. In addition, the quality of the asymptotic approximation does not seem uniform over all the components of the hydrodynamic function matrix.

Note that we do not expect to recover the exact hydrodynamic function behavior over such a broad range of frequency as that presented, with only a three term expansion as in Eq. (D.7). For comparison, note that in [1], the correction alone for a thin rectangular versus circular cross section was presented in terms of a (6,6)-order Padé approximant valid over ten decades of nondimensional frequency. Although we do not further pursue the hydrodynamics in the extremely low frequency range in this paper, the value of Eq. (D.7) is also to provide an alternative, numerically stable way to calculate the modal hydrodynamic function matrix in the very low β range, where the approach described in Sec. 3 becomes numerically ill-conditioned and slowly convergent.

Acknowledgments

This material is based in part on work supported by the National Science Foundation under Grant No. 1847513. The authors would like to thank the anonymous reviewers for their careful reading of the manuscript and for giving useful suggestions that have helped improve the work and its presentation.

References

- [1] J. E. Sader, Frequency response of cantilever beams immersed in viscous fluids with applications to the atomic force microscope, Journal of Applied Physics 84 (1) (1998) 64–76.
- [2] A. Maali, C. Hurth, R. Boisgard, C. Jai, T. Cohen-Bouhacina, J.-P. Aimé, Hydrodynamics of oscillating atomic force microscopy cantilevers in viscous fluids, Journal of Applied Physics 97 (7) (2005) 074907.
- [3] R. Clarke, O. Jensen, J. Billingham, Three-dimensional elastohydrodynamics of a thin plate oscillating above a wall, Physical Review E 78 (5) (2008) 056310.
- [4] R. C. Tung, J. P. Killgore, D. C. Hurley, Liquid contact resonance atomic force microscopy via experimental reconstruction of the hydrodynamic function, Journal of Applied Physics 115 (22) (2014) 224904.
- [5] M. Kimber, S. V. Garimella, Measurement and prediction of the cooling characteristics of a generalized vibrating piezoelectric fan, International Journal of Heat and Mass Transfer 52 (19-20) (2009) 4470–4478.
- [6] A. Eastman, J. Kiefer, M. Kimber, Thrust measurements and flow field analysis of a piezoelectrically actuated oscillating cantilever, Experiments in Fluids 53 (2012) 1533–1543.
- [7] I. Dufour, E. Lemaire, B. Caillard, H. Debéda, C. Lucat, S. M. Heinrich, F. Josse, O. Brand, Effect of hydrodynamic force on microcantilever vibrations: Applications to liquid-phase chemical sensing, Sensors and Actuators B: Chemical 192 (2014) 664–672.
- [8] T. Manzaneque, V. Ruiz-Díez, J. Hernando-García, E. Wistrela, M. Kucera, U. Schmid, J. L. Sánchez-Rojas, Piezoelectric MEMS resonator-based oscillator for density and viscosity sensing, Sensors and Actuators A: Physical 220 (2014) 305–315.
- [9] S. Michelin, S. G. Llewellyn Smith, Resonance and propulsion performance of a heaving flexible wing, Physics of Fluids 21 (7) (2009) 071902.
- [10] A. Eastman, M. L. Kimber, Flow shaping and thrust enhancement of sidewall bounded oscillating cantilevers, International Journal of Heat and Fluid Flow 48 (2014) 35–42.
- [11] A. J. Richards, P. Oshkai, Effect of the stiffness, inertia and oscillation kinematics on the thrust generation and efficiency of an oscillating-foil propulsion system, Journal of Fluids and Structures 57 (2015) 357–374.
- [12] S. B. Behbahani, X. Tan, Bio-inspired flexible joints with passive feathering for robotic fish pectoral fins, Bioinspiration & Biomimetics 11 (3) (2016) 036009.
- [13] A. Dryden, M. Ballard, Numerical investigation of a biomimetic elastic valve for microfluidic pumping, Journal of Fluids and Structures 103 (2021) 103265.
- [14] A. Ihara, H. Watanabe, On the flow around flexible plates, oscillating with large amplitude, Journal of Fluids and Structures 8 (7) (1994) 601–619.
- [15] S. M. Wait, S. Basak, S. V. Garimella, A. Raman, Piezoelectric fans using higher flexural modes for electronics cooling applications, IEEE Transactions on Components and Packaging Technologies 30 (1) (2007) 119–128.
- [16] R. A. Bidkar, M. Kimber, A. Raman, A. K. Bajaj, S. V. Garimella, Nonlinear aerodynamic damping of sharp-edged flexible beams oscillating at low Keulegan-Carpenter numbers, Journal of Fluid Mechanics 634 (2009) 269–289.
- [17] G. M. Gilson, S. J. Pickering, D. B. Hann, C. Gerada, Piezoelectric fan cooling: A novel high reliability electric machine thermal management solution, IEEE Transactions on Industrial Electronics 60 (11) (2013) 4841–4851.

- [18] H. D. Akaydin, N. Elvin, Y. Andreopoulos, Energy harvesting from highly unsteady fluid flows using piezoelectric materials, Journal of Intelligent Material Systems and Structures 21 (13) (2010) 1263–1278.
- [19] M. Aureli, C. Prince, M. Porfiri, S. D. Peterson, Energy harvesting from base excitation of ionic polymer metal composites in fluid environments, Smart Materials and Structures 19 (1) (2010) 015003.
- [20] D. T. Akcabay, Y. L. Young, Hydroelastic response and energy harvesting potential of flexible piezoelectric beams in viscous flow, Physics of Fluids 24 (5) (2012) 054106.
- [21] Y. Cha, W. Chae, H. Kim, H. Walcott, S. D. Peterson, M. Porfiri, Energy harvesting from a piezoelectric biomimetic fish tail, Renewable Energy 86 (2016) 449–458.
- [22] E. O. Tuck, Calculation of unsteady flows due to small motions of cylinders in a viscous fluid, Journal of Engineering Mathematics 3 (1969) 29–44.
- [23] W. H. Chu, Technical report no. 2dtmb, contract nobs-86396 (x), Tech. rep., Southwest Research Institute, San Antonio, Texas (1963).
- [24] C. P. Green, J. E. Sader, Torsional frequency response of cantilever beams immersed in viscous fluids with applications to the atomic force microscope, Journal of Applied Physics 92 (10) (2002) 6262–6274.
- [25] C. P. Green, J. E. Sader, Small amplitude oscillations of a thin beam immersed in a viscous fluid near a solid surface, Physics of Fluids 17 (7) (2005) 073102.
- [26] G. Di Ilio, I. Sahin, A. Tafuni, Unsteady Stokes flow for a vibrating cantilever under a free-surface, in: Proceedings of the ASME 2014 International Mechanical Engineering Congress and Exposition (IMECE 2014), Montreal, Canada, 2014, p. V009T12A003.
- [27] D. R. Brumley, M. Willcox, J. E. Sader, Oscillation of cylinders of rectangular cross section immersed in fluid, Physics of Fluids 22 (5) (2010) 052001
- [28] M. Aureli, M. Porfiri, Low frequency and large amplitude oscillations of cantilevers in viscous fluids, Applied Physics Letters 96 (16) (2010) 164102.
- [29] M. Aureli, M. E. Basaran, M. Porfiri, Nonlinear finite amplitude vibrations of sharp-edged beams in viscous fluids, Journal of Sound and Vibration 331 (7) (2012) 1624–1654.
- [30] A. Tafuni, I. Sahin, Non-linear hydrodynamics of thin laminae undergoing large harmonic oscillations in a viscous fluid, Journal of Fluids and Structures 52 (2015) 101–117.
- [31] U. S. Lindholm, D. D. Kana, W. H. Chu, H. A. Abramson, Elastic vibration characteristics of cantilever plates in water, Journal of Ship Research 9 (02) (1965) 11–36.
- [32] C. Atkinson, M. M. de Lara, The frequency response of a rectangular cantilever plate vibrating in a viscous fluid, Journal of Sound and Vibration 300 (1-2) (2007) 352–367.
- [33] A. L. Facci, M. Porfiri, Analysis of three-dimensional effects in oscillating cantilevers immersed in viscous fluids, Journal of Fluids and Structures 38 (2013) 205–222.
- [34] N. Shen, D. Chakraborty, J. E. Sader, Resonant frequencies of cantilevered sheets under various clamping configurations immersed in fluid, Journal of Applied Physics 120 (14) (2016) 144504.
- [35] A. Gesing, D. Platz, U. Schmid, A numerical method to determine the displacement spectrum of micro-plates in viscous fluids, Computers and Structures 260 (2022) 106716.
- [36] A. Gesing, D. Platz, U. Schmid, Viscous fluid-structure interaction of micro-resonators in the beam-plate transition, Journal of Applied Physics 131 (13) (2022) 134502.
- [37] N. Shen, D. Chakraborty, J. E. Sader, Frequency response of cantilevered plates of small aspect ratio immersed in viscous fluids, Journal of Applied Physics 133 (3) (2023) 034501.
- [38] C. Castille, I. Dufour, C. Lucat, Longitudinal vibration mode of piezoelectric thick-film cantilever-based sensors in liquid media, Applied Physics Letters 96 (15) (2010) 154102.
- [39] M. Aureli, S. N. Ahsan, R. H. Shihab, R. C. Tung, Plate geometries for contact resonance atomic force microscopy: Modeling, optimization, and verification, Journal of Applied Physics 124 (1) (2018) 014503.
- [40] F. Patocka, M. Schlögl, C. Schneidhofer, N. Dörr, M. Schneider, U. Schmid, Piezoelectrically excited MEMS sensor with integrated planar coil for the detection of ferrous particles in liquids, Sensors and Actuators B: Chemical 299 (2019) 126957.
- [41] M. Aureli, R. Tung, A plate-like sensor for the identification of sample viscoelastic properties using contact resonance atomic force microscopy, ASME Letters in Dynamic Systems and Controls 1 (3) (2021) 031008.
- [42] R. Shihab, T. Jalil, B. Gulsacan, M. Aureli, R. Tung, Sensor egregium—an atomic force microscope sensor for continuously variable resonance amplification, ASME Journal of Vibration and Acoustics 143 (4) (2021) 041013.
- [43] S. N. Ahsan, M. Aureli, Nonlinear oscillations of shape-morphing submerged structures: Control of hydrodynamic forces and power dissipation via active flexibility, Journal of Fluids and Structures 74 (2017) 35–52.
- [44] S. N. Ahsan, M. Aureli, Small amplitude oscillations of a shape-morphing plate immersed in a viscous fluid near a solid wall, Journal of Applied Physics 124 (13) (2018) 134502.
- [45] S. N. Ahsan, M. Aureli, Finite amplitude torsional oscillations of shape-morphing plates immersed in viscous fluids, Physics of Fluids 32 (5) (2020) 053101.
- [46] S. N. Ahsan, M. Aureli, Three-dimensional analysis of hydrodynamic forces and power dissipation in shape-morphing cantilevers oscillating in viscous fluids, International Journal of Mechanical Sciences 149 (2018) 436–451.
- [47] P. Bearman, M. Downie, J. Graham, E. Obasaju, Forces on cylinders in viscous oscillatory flow at low Keulegan-Carpenter numbers, Journal of Fluid Mechanics 154 (1985) 337–356.
- [48] T. Sarpkaya, Force on a circular cylinder in viscous oscillatory flow at low Keulegan-Carpenter numbers, Journal of Fluid Mechanics 165 (1986) 61–71.
- [49] J. Morison, J. Johnson, S. Schaaf, et al., The force exerted by surface waves on piles, Journal of Petroleum Technology 2 (05) (1950) 149–154.
- [50] T. Sarpkaya, On the parameter $\beta = \text{Re/KC} = D^2/\nu T$, Journal of Fluids and Structures 21 (4) (2005) 435–440.
- [51] C. Pozrikidis, A singularity method for unsteady linearized flow, Physics of Fluids A: Fluid Dynamics 1 (9) (1989) 1508-1520.
- [52] J. N. Reddy, Energy and variational methods in applied mechanics, Wiley, New York, 1991.

- [53] T. Mura, T. Koya, Variational methods in mechanics, Oxford University Press, New York, NY, 1992.
- [54] M. Aureli, C. Pagano, M. Porfiri, Nonlinear finite amplitude torsional vibrations of cantilevers in viscous fluids, Journal of Applied Physics 111 (12) (2012) 124915.
- [55] C.-Y. Wang, On high-frequency oscillatory viscous flows, Journal of Fluid Mechanics 32 (1968) 55-68.
- [56] L. Meirovitch, Dynamics and Control of Structures, Wiley-Interscience, New York, NY, 1990.
- [57] F. Axisa, J. Antunes, Modelling of Mechanical Systems: Fluid-Structure Interaction, Vol. 3, Butterworth-Heinemann, Oxford, UK, 2007.
- [58] S. Güttel, F. Tisseur, The nonlinear eigenvalue problem, Acta Numerica 26 (2017) 1-94.
- [59] B. Gulsacan, M. Aureli, Underwater oscillations of rigid plates with H-shaped cross sections: An experimental study to explore their flow physics, Physics of Fluids 35 (3) (2023) 033102.
- [60] L. Meirovitch, Analytical methods in vibrations, MacMillan, London, 1967.
- [61] J. C. R. Hunt, A. A. Wray, P. Moin, Eddies, stream, and convergence zones in turbulent flows, Proceedings of the Summer Program CTR-S88 (1988) 193–208.
- [62] Tracker video analysis and modeling tool for physics education (2023). URL https://physlets.org/tracker/
- [63] Online materials information resource MatWeb (2023). URL https://www.matweb.com/index.aspx
- [64] S. Basak, A. Raman, Hydrodynamic coupling between micromechanical beams oscillating in viscous fluids, Physics of Fluids 19 (1) (2007) 017105.
- [65] A. K. Manickavasagam, S. Gutschmidt, M. Sellier, Interactive fluid coupling effects of non-neighbouring members, Sensors 21 (21) (2021) 6961.
- [66] S. P. Timoshenko, S. Woinowsky-Krieger, Theory of plates and shells, McGraw-Hill, 1959.
- [67] E. H. Dowell, On asymptotic approximations to beam model shapes, ASME Journal of Applied Mechanics 51 (2) (1984) 439.
- [68] M. A. Hopcroft, W. D. Nix, T. W. Kenny, What is the Young's modulus of silicon?, Journal of Microelectromechanical Systems 19 (2) (2010) 229–238.
- [69] J. N. Reddy, Mechanics of laminated composite plates: Theory and analysis, CRC Press, Boca Raton, FL, 1997.
- [70] A. W. Leissa, Vibration of plates, Office of Technology Utilization, NASA, Washington, D.C., 1969.
- [71] R. P. Kanwal, An integral equation perturbation technique in applied mathematics, Journal of Mathematics and Mechanics 19 (7) (1970) 625–656
- [72] E. M. Purcell, Life at low Reynolds number, American Journal of Physics 45 (1) (1977) 3–11.
- [73] G. G. Stokes, On the effect of the internal friction of fluids on the motion of pendulums, Transactions of the Cambridge Philosophical Society 9 (1851) 1–141.
- [74] L. Rosenhead (Ed.), Laminar Boundary Layers, Dover, New York, NY, 1988.